ARTICLE IN PRESS

Computers and Mathematics with Applications xxx (xxxx) xxx

Contents lists available at ScienceDirect

Computers and Mathematics with Applications

journal homepage: www.elsevier.com/locate/camwa

New applications of numerical simulation based on lattice Boltzmann method at high Reynolds numbers

Bo An [a,*], J.M. Bergadà [a], F. Mellibovsky [b], W.M. Sang [c]

[a] Department of Fluid Mechanics, Universitat Politécnica de Catalunya, 08034, Barcelona, Spain
[b] Department of Physics, Aerospace Engineering Division, Universitat Politécnica de Catalunya, 08034, Barcelona, Spain
[c] School of Aeronautics, Northwestern Polytechnical University, Xi'an, China

ARTICLE INFO

Article history:
Received 29 May 2019
Received in revised form 30 September 2019
Accepted 3 October 2019
Available online xxxx

Keywords:
Lattice Boltzmann method
Large eddy simulation
Multiple-relaxation time
Wall driven cavity
Flow over obstacles
Tree grid

ABSTRACT

In order to study the flow behavior at high Reynolds numbers, two modified models, known as the multiple-relaxation-time lattice Boltzmann method (MRT-LBM) and large-eddy-simulation lattice Boltzmann method (LES-LBM), have been employed in this paper. The MRT-LBM was designed to improve numerical stability at high Reynolds numbers, by introducing multiple relaxation time terms, which consider the variations of density, energy, momentum, energy flux and viscous stress tensor. As a result, MRT-LBM is capable of dealing with turbulent flows considering energy dispersion and dissipation. In the present paper, this model was employed to simulate the flow at turbulent Reynolds numbers in wall-driven cavities. Two-sided wall driven cavity flow was studied for the first time, based on MRT-LBM, at Reynolds numbers ranging from 2×10^4to1×10^6, and employing a very large resolution2048×2048. It is found that whenever top and bottom lids are moving in the opposite directions, and the Reynolds number is higher than 2×10^4, the flow is chaotic, although some quasi-symmetric properties still remain, fully disappearing at Reynolds numbers between 2×10^5 and 3×10^5. Furthermore, between this Reynolds numbers range, $2 \times 10^5 < Re < 3 \times 10^5$, the quasi-symmetric structures turn into a much smaller and fully chaotic eddies. The LES-LBM model implements the large eddy simulation turbulent model into the conventional LBM, allowing to study the flow at turbulent Reynolds numbers. LES-LBM combined with Quadruple-tree Cartesian cutting grid (tree grid) was employed for the first time to characterize the flow dynamics over a cylinder and a hump, at relatively high Reynolds numbers. In order to construct the macroscopic quantities in the virtual boundaries separating two different grid levels, a set of new schemes were designed. The coupling of the LES-LBM and tree grid drastically reduced the computational time required to perform the simulations, thus, allowing to minimize the hardware requirements. LES-LBM model is shown to be much more efficient when combined with the tree grid instead of using the standard Cartesian grid.

1. Introduction

1.1. Numerical stability associated to the LBM at high Reynolds numbers

As a vigorous and rational numerical methodology, the lattice Boltzmann method was originated and evolved from the lattice gas automata (LGA) [1]. Due to the continuous developments made by researchers [2,3], the lattice

* Corresponding author.
E-mail address: bo_alan_an@163.com (B. An).

https://doi.org/10.1016/j.camwa.2019.10.002
0898-1221/

Nomenclature (all parameters are non-dimensional)

$\vec{a}$	Acceleration of molecules
c_s	Sound speed
c	Lattice velocity
C	Constant of Smagorinsky eddy
C_P	Temporal pressure coefficient
C_L	Lift coefficient
C_D	Drag coefficient
C_f	Skin friction coefficient
D	Space dimension
d_D	Particle diameter
$\vec{e}_\alpha$	Unit velocities vector along discrete directions
E	Macroscopic quantity, internal energy
$\vec{g}$	The vertical component of velocity vector difference
F_x	x components of total body force of the object
F_y	y components of total body force of the object
$f(\vec{r}, \vec{\xi}, t)$	Distribution function
$f^{eq}(\vec{r}, \vec{\xi})$	Equilibrium distribution function
$\mathrm{F}_1, \mathrm{F}_2$	Post-collision distribution function of two fluid particles
f_1, f_2	Pre-collision distribution function of two fluid particles
f_α	Discrete distribution functions on α directions
F_α	Discrete distribution functions on α directions after collision
$f_\alpha(\vec{r} + \vec{e}_\alpha \Delta t, t + \Delta t)$	Discrete-post collision distribution functions vector
$f_\alpha(\vec{r}, t)$	Discrete-pre collision distribution functions vector
$\vec{f}_\alpha^{eq}$	Nine-ordered vector of discrete equilibrium distribution functions
$\vec{f}_\alpha'$	Discrete distribution functions vector after collision
f_α^{neq}	The non-equilibrium state of distribution functions
f_α^{v}	Virtual distribution functions
f_α^{ev}	The virtual equilibrium distribution functions
f_α^{nev}	The virtual non-equilibrium distribution functions
L	Characteristic length
$\vec{m}_\alpha$	Momentum vector
$\vec{m}_\alpha{}^{eq}$	Equilibrium momentum vector
$\vec{M}_{\alpha\beta}$	Switch matrix
$\vec{m}_\alpha'$	Momentum vector after collision
N	Number of cells along x and y axis
p	Surface static pressure
p_∞	Free stream static pressure
Re	Reynolds number
R	Gas constant
$\vec{r}$	Spatial position vector
$\vec{r}_b$	Spatial position of point ***b***
$\vec{r}_w$	Spatial position of point ***w***
$\vec{r}_c$	Spatial position of point ***c***
$\vec{r}_a$	Spatial position of point ***a***
$\vec{S}_{\alpha\beta}$	A diagonal matrix
$\lvert\vec{S}_{ij}\rvert$	Magnitude of large scale strain rate tensor
t	Time

Boltzmann method gradually improved as a mature methodology. It turned out that the lattice Boltzmann method is numerically capable of solving many mathematical and physical problems, including model PDEs [4,5], thermodynamics problems [6,7], combustion [8,9], fluid mechanics [10,11], and other research applications.

Please cite this article as: B. An, J.M. Bergadà, F. Mellibovsky et al., New applications of numerical simulation based on lattice Boltzmann method at high Reynolds numbers, Computers and Mathematics with Applications (2019), https://doi.org/10.1016/j.camwa.2019.10.002.

T	Temperature
$T2$	Computational time per time unit with standard Cartesian grid
$T1$	Computational time per time unit with tree grid
$\vec{u}$	Macroscopic quantity, velocity
$\vec{u}_b$	Velocity of point $\boldsymbol{b}$
$\vec{u}_w$	Velocity of point $\boldsymbol{w}$
$\vec{u}_a$	Velocity of point $\boldsymbol{a}$
$\vec{u}_c$	Velocity of point $\boldsymbol{c}$
U	Initial velocity of the flow field
U_d	Wall driven velocity
U_x	Horizontal component of velocity
U_y	Vertical component of velocity
U_∞	Far field velocity
α, β	Discrete directions (from 0 to 8 in the present LBGK *D2Q9* model)
χ	Parameter to be determined
Δx	Grid spacing
Δt	Time step
Δx_n	Grid spacing of nth grid level
Δx_0	Grid spacing of root grid
Δ_e	Embed depth
Δx_{coarse}	Grid spacing of coarse grid
Δx_{fine}	Grid spacing of fine grid
Δ_f	Filter scale
ψ	Function of macroscopic quantities
ν	Kinematic viscosity of laminar flow
ν_t	Kinematic viscosity of turbulence flow
ν_{total}	Total kinematic viscosity
$\overline{\Pi}_{i,j}$	Non-equilibrium stress tensor
ρ	Macroscopic quantity, density
ρ_0	Initial density
τ	Single relaxation time term
τ_{total}	Total relaxation time
τ_{lid}	Shear stresses on the lid
Ω_f	Collision operator
Ω_f^α	Discrete collision operator on α directions
$d\Theta$	Integral infinitesimal of angle
ω_α	Weight Coefficients
$\vec{\xi}$	Velocity vector of molecules
$\vec{\xi}_1 - \vec{\xi}_2$	Vectorial difference of velocity
χ	Linear interpolation factor
$\Lambda_{\alpha\beta}$	Collision matrix

From previous researchers' work [12–22], it is noticed that LBM applicability was mostly limited to low Reynolds numbers due to a deficiency of lattice Boltzmann method, known as the numerical instability. Besides, the numerical applications of the original LBM at high Reynolds numbers, require a very high grid resolution [23]. Many studies have shown that the numerical stability of LBM deteriorates as the Reynolds number increases [12–22].

Providing the grid spacing remains constant, the original LBM relaxation time τ approaches 0.5 as Reynolds number increases, and according to [2,3], numerical stability is being compromised. The numerical stability of LBM can-be improved through grid refinement, but this is impractical, especially at very large Reynolds numbers. A great deal of research had been done to improve the stability behavior of LBM at high Reynolds numbers. Several ways to mitigate the issue are the entropic lattice Boltzmann Method [24,25], the regularized lattice Boltzmann method [26,27], the multiple relaxation time LBM (MRT-LBM) [12–17], and the large eddy simulation LBM (LES-LBM) [18–22]. In the present paper, the MRT-LBM and LES-LBM were used to improve the numerical stability of conventional LBM at high Reynolds numbers. In order to further optimize the lattice Boltzmann method, the quadruple-tree Cartesian cutting grid (tree grid), generated by the local grid refinement technology, was also employed in this paper.

Please cite this article as: B. An, J.M. Bergadà, F. Mellibovsky et al., New applications of numerical simulation based on lattice Boltzmann method at high Reynolds numbers, Computers and Mathematics with Applications (2019), https://doi.org/10.1016/j.camwa.2019.10.002.

In the present paper, several numerical examples were initially evaluated to validate the in-house code. The multiple-relaxation-time lattice Boltzmann method applied to the numerical simulation of wall-driven cavities at high Reynolds numbers, including three different flow driving conditions, cases (a), (b) and (c) were considered. Case (a) represents the usual lid-driven cavity, case (b) characterizes the top and bottom wall-driven cavity moving in the same direction and case (c) describes the cavity flow with the top and bottom walls moving in opposite directions. Considering case (a) at high Reynolds numbers, the results delivered by Chai et al. [22], where the multiple-relaxation-time lattice Boltzmann method was used to simulate the lid-driven cavity flow at high Reynolds numbers, were used for comparison. The evaluation of cases (b) and (c) at high Reynolds numbers, via employing MRT-LBM are completely new and they are presented in this paper for the first time. Notice that these two particular geometries at Reynolds numbers up to 2000, were previously studied by Perumal and Dass [23] using the conventional lattice Boltzmann method.

Via using the novel LES-LBM combined with Quadruple-tree Cartesian cutting grid (tree grid), the flow around two different bluff bodies, a cylinder and a hump, at relatively high Reynolds numbers was evaluated. It is important to highlight that the coupling between LES-LBM and tree grid, required the use of a set of new schemes in order to be able to construct the macroscopic quantities in the virtual boundaries. When considering the flow over a hump, in the present paper, the new results obtained from the present in-house code were compared with the results introduced by Suzuki [28] at Reynolds number, 4000. He investigated in 2D at Reynolds number 4000 the compressible unsteady, laminar flow over a hump by using direct numerical simulation. Body forces as well as vortex shedding were analyzed.

When considering the cylinder case, the results of the flow past a cylinder at Reynolds number 100, were compared with the ones obtained by other researchers [29–32]. Ding et al. [29] investigated 2D circular cylinders arranged in tandem and side-by-side via using the mesh free least square-based finite difference method at Reynolds numbers 100 and 200. Meneghini et al. [30] studied the 2D circular cylinders via using a fractional step method at Reynolds numbers 100 and 200. In order to have a better description of the boundary layer, they used a very fine mesh close to the cylinder wall. Harichandan and Roy [31], solved the Navier–Stokes equations by the finite volume method, to simulate the flow past an array of two and three cylinders located in parallel and in tandem. The single cylinder case was also run and compared at two different Reynolds numbers 100 and 200. Behara and Mittal [32], numerically studied the oblique shedding generated by the flow past a 2D circular cylinder via using stabilized finite element method at three Reynolds numbers 60, 100 and 150.

The flow over a cylinder at Reynolds number 3900 was employed to further study the LES-LBM coupled with tree grid in-house code advantages. The comparison between the present prediction and previous research undertaken at Reynolds number 3900 by [33–41] is presented in Section 5. In the research done by Beaudan and Moin [33], Mittal and Moin [34], Kravchenko and Moin [35] and You and Moin [37], they evaluated a modified Smagorinsky sub-grid-scale eddy-viscosity model, which was implemented in the LES turbulent model. They also checked the accuracy of the upwind-biased, central finite-difference and B-splines numerical methods, observing that the B-splines method agrees better with the experimental results. Lehmkuhl et al. [36], carefully studied in 3D via direct numerical simulation, the downstream vortex shedding on a circular cylinder at Reynolds number 3900. They observed the large-scale quasi-periodic motion seems to be related with the modulation of the recirculation bubble, which causes its shrinking and enlargement over time. As previously done by You and Moin, [37], Rajani et al. [38], applied the Smagorinsky sub-grid scale algorithm implemented in the LES turbulent model, their simulations were based on assessing the limitation and accuracy level of the present algorithm. Comparisons with a large number of previous researchers work were made. Pereira et al. [39] simulated the flow past a circular cylinder at the same Reynolds number via using 2D and 3D RANS, DDES and XLES models. They observed the three dimensional DDES and XLES models produced more accurate results. Wang et al. [40], proposed a 2D numerical large eddy simulation (LES) method combined with the characteristic-based operator-splitting finite element method, to solve Navier–Stokes equations at Reynolds number 3900. In Breuer [41], two sub-grid scale models (Smagorinsky and dynamic model) coupled with LES were employed, also the LES model without any sub-grid model was evaluated. Their work focused in evaluating numerical and modeling aspects affecting the LES simulations. Different resolutions were considered.

1.2. Original lattice Boltzmann equations

In what follows, a brief description of the original LBM is presented, this introduction will be later used to implement the MRT-LBM and LES-LBM methodologies. The continuous Boltzmann equation is given by Eq. (1), notice that all parameters presented in this equation, as well as the ones introduced in the rest of the equations presented in this paper are non-dimensional. As in many previous applications [10,11,14,17,21], the very common binary collision assumption is employed in the present paper to obtain Eq. (1).

$$\frac{\partial f(\vec{r},\vec{\xi},t)}{\partial t}+\vec{\xi}\cdot\frac{\partial f(\vec{r},\vec{\xi},t)}{\partial \vec{r}}+\vec{a}\cdot\frac{\partial f(\vec{r},\vec{\xi},t)}{\partial \vec{\xi}}=\iint(\mathrm{F}_1\mathrm{F}_2-f_1f_2)d_D^2\left|\vec{g}\right|\cos\theta d\Theta d\vec{\xi}_1 \tag{1}$$

The term $f(\vec{r},\vec{\xi},t)$ is called the distribution function, $\vec{r}$ is the spatial position vector, t is the non-dimensional time, $\vec{\xi}$ is the velocity vector, $\vec{a}$ is the particle acceleration, d_D is the particle diameter, F_1, F_2 and f_1, f_2 are the post- and pre- collision distribution functions of two fluid particles, $\vec{g}$ is the vertical component of $\vec{\xi}_1-\vec{\xi}_2$ and $d\Theta$ is the angle differential. The

Please cite this article as: B. An, J.M. Bergadà, F. Mellibovsky et al., New applications of numerical simulation based on lattice Boltzmann method at high Reynolds numbers, Computers and Mathematics with Applications (2019), https://doi.org/10.1016/j.camwa.2019.10.002.

left hand side of Eq. (1) represents the streaming term, the right hand side represents an integral-differential term, which is called the collision term. To simplify the collision term, Bhatnagar Gross and Krook [42], presented the famous BGK approximation, where the collision term was replaced by a simple collision operator Ω_f, as a result, the Boltzmann–BGK equation reads

$$\frac{\partial f(\vec{r},\vec{\xi},t)}{\partial t}+\vec{\xi}\cdot\frac{\partial f(\vec{r},\vec{\xi},t)}{\partial \vec{r}}+\vec{a}\cdot\frac{\partial f(\vec{r},\vec{\xi},t)}{\partial \vec{\xi}}=\Omega_f=\frac{1}{\tau}\left[f^{eq}(\vec{r},\vec{\xi})-f(\vec{r},\vec{\xi},t)\right] \tag{2}$$

where τ is the singular relaxation time term and $f^{eq}(\vec{r},\vec{\xi})$ is the equilibrium distribution function.

Discretizing Eq. (2) both in space and time, the lattice Boltzmann equation is obtained as

$$f_\alpha(\vec{r}+\vec{e}_\alpha\Delta t,t+\Delta t)-f_\alpha(\vec{r},t)=\Omega_f^\alpha=\frac{1}{\tau}\left[f_\alpha^{eq}(\vec{r},\vec{\xi})-f_\alpha(\vec{r},\vec{\xi},t)\right] \tag{3}$$

where α represents the direction of discrete velocities, $f_\alpha(\vec{r}+\vec{e}_\alpha\Delta t,t+\Delta t)$ and $f_\alpha(\vec{r},t)$ are the discrete-post and -pre collision distribution functions vector and Ω_f^α is the discrete collision operator in direction α. Notice that, the external forces term is neglected from Eqs. (1)–(3), since in the present applications, no external forces are involved. It is common knowledge that the Navier–Stokes equations are recovered from the discrete lattice Boltzmann equation [11,20,43,44]. In order to solve fluid-flow related problems, the physical quantities, density ρ, velocity $\vec{u}$ and internal energy E, must be defined as [45]

$$\begin{cases}\rho=\sum_\alpha f_\alpha\\ \rho\vec{u}=\sum_\alpha \vec{e}_\alpha f_\alpha\\ \rho E=\dfrac{\rho DRT}{2}\sum_\alpha(\vec{e}_\alpha-\vec{u})^2 f_\alpha\end{cases} \tag{4}$$

where D is the space dimension, R is the non-dimensional gas constant and T refers to the non-dimensional temperature.

The LBGK model for solving the Navier–Stokes equations was presented by Qian et al. [11], and it is one of the most popular models used in LBM when applied to fluid dynamics problems. This model is also employed in the present paper. According to Qian et al. [11], the equilibrium distribution functions, for the 9 discrete velocities (9-bit model), are determined by

$$f_\alpha^{eq}=\omega_\alpha\rho\left[1+\frac{\vec{e}_\alpha\cdot\vec{u}}{{c_s}^2}+\frac{(\vec{e}_\alpha\cdot\vec{u})^2}{2{c_s}^4}-\frac{u^2}{2{c_s}^2}\right]\quad \alpha=0,1,\ldots,8 \tag{5}$$

where ω_α are the weight coefficients, and c_s is the non-dimensional sound speed. The discrete velocities of LBGK two dimensional 9-bit model *D2Q9* are given by

$$\vec{e}=c\begin{bmatrix}0&1&0&-1&0&1&-1&-1&1\\0&0&1&0&-1&1&1&-1&-1\end{bmatrix}$$
$$c_s=\tfrac{c}{\sqrt{3}}\qquad \omega_\alpha=\begin{cases}4/9 & \vec{e}_\alpha^2=0\\ 1/9 & \vec{e}_\alpha^2=c^2\\ 1/36 & \vec{e}_\alpha^2=2c^2\end{cases} \tag{6}$$

where $c=\Delta x/\Delta t=1$ is the non-dimensional lattice velocity, and Δx, Δt are the lattice grid non-dimensional spacing and the non-dimensional time step respectively.

Fig. 1 shows the discrete velocities of the LBGK *D2Q9* model employed in all simulations presented in this paper.

2. Mesh

2.1. Standard Cartesian grid

The application of standard Cartesian grid is very common in LBM, because of its particular structural advantages that fit the streaming-collision theory of LBM. The standard Cartesian grid, however, usually generates a huge computational burden, involving long computational time and high hardware requirements, therefore restricting LBM applications. Nevertheless, for simple geometries, the standard Cartesian grid is widely employed, and in the present paper it will be used to evaluate the flow inside wall-driven cavities. Two main cases are presented in this paper, the classic lid-driven cavity flow, case (a), which will be compared with the results presented by Chai et al. [12], and the two-sided wall-driven cavity flow, cases (b) and (c). The resolution used for case (a), was 512×512, being this resolution the one already used in reference [12]. The mesh resolution employed to evaluate the flow inside the two-sided wall-driven cavity, was of 2048×2048 for all the Reynolds numbers evaluated. Notice that this mesh is four times denser than the largest one used in reference [12]. Considering the simulation of complex geometries with high Reynolds numbers, the mesh refinement

Please cite this article as: B. An, J.M. Bergadà, F. Mellibovsky et al., New applications of numerical simulation based on lattice Boltzmann method at high Reynolds numbers, Computers and Mathematics with Applications (2019), https://doi.org/10.1016/j.camwa.2019.10.002.

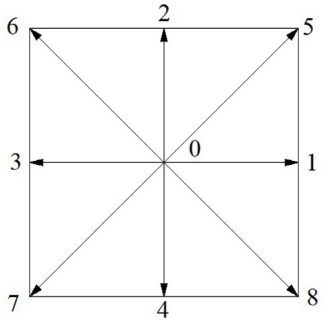

Fig. 1. Discrete velocities of lattice Boltzmann *D2Q9* model.

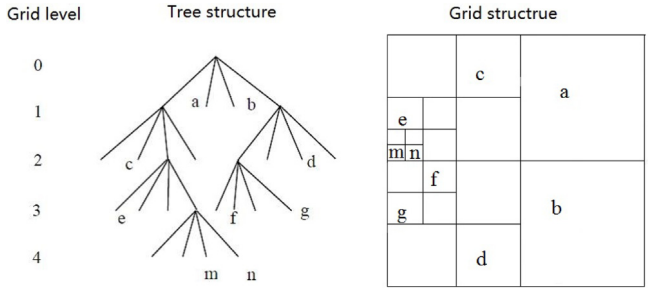

Fig. 2. Quadruple-tree structure and grid generation.

is an essential point to be considered, yet, a blind and undisciplined refinement through the whole domain is illogical and impractical, as computational resources are poorly used. Technically, the refinement is required in the regions where fluid variables are expected to suffer severe temporal or spatial changes.

2.2. Quadruple-tree Cartesian cutting grid (tree grid)

The tree grid is a typical example of Cartesian non-uniform grid. More and more researchers are employing such grid, due to its excellent merits shown in many practical applications [46,47].

In this paper, the tree grid was employed in the numerical simulations launched using LES-LBM. As required by the cell structure, a given cell zone was divided into several levels with different grid/cell spacing, the grid spacing changed in each grid level. In the present paper, the models studied were two dimensional, the quadruple-tree structure [46,47], was employed to generate the tree grid. The basic idea is that a flow field is viewed as a big single cell, known as the root cell, and via using the theory of tree grid, it generates 2^2 sub-cells (2^3 in three dimensions). In the next step of the process, each of these four sub-cells also generates another four sub-cells. Through this loop, the final mesh of the whole flow field was accomplished. Fig. 2 shows the quadruple-tree structure and the process of grid generation.

The grid level at the left side of Fig. 2 presents different degrees of grid refinement. It is to be noticed that the root cell is defined as level 0. The grid spacing of each grid level [48–50] is to be obtained by Eq. (7), which is written as

$$\Delta x_n = \Delta x_0 / 2^n \tag{7}$$

where Δx_n refers to the grid spacing of the nth grid level and Δx_0 is the grid spacing of the root cell. Fig. 3 shows the tree grid of a cylinder and a hump, which will be employed in Section 5.1 to evaluate the flow around these obstacles. It is important to notice that both obstacles, a circular cylinder and a hump, have the same characteristic length $L = 1.0$. The total mesh cells were, 16 652 for the flow past a circular cylinder and 55 748 for the flow over a hump. In the same figure, are also presented the boundary conditions employed for these two geometries. At the inlet, Dirichlet boundary conditions for all variables were used. At the outlet and far-field boundaries, Neumann boundary conditions for density and U_x velocity were used, Dirichlet boundary conditions for U_y velocity were employed. In all walls, Dirichlet boundary conditions for velocities and Neumann boundary conditions for density were used.

3. Mathematical background of the methodologies employed

The original lattice Boltzmann method is usually applied to simulate incompressible flow, being the Reynolds number commonly limited to low values. In order to clarify why the numerical stability deteriorates at high Reynolds numbers,

Please cite this article as: B. An, J.M. Bergadà, F. Mellibovsky et al., New applications of numerical simulation based on lattice Boltzmann method at high Reynolds numbers, Computers and Mathematics with Applications (2019), https://doi.org/10.1016/j.camwa.2019.10.002.

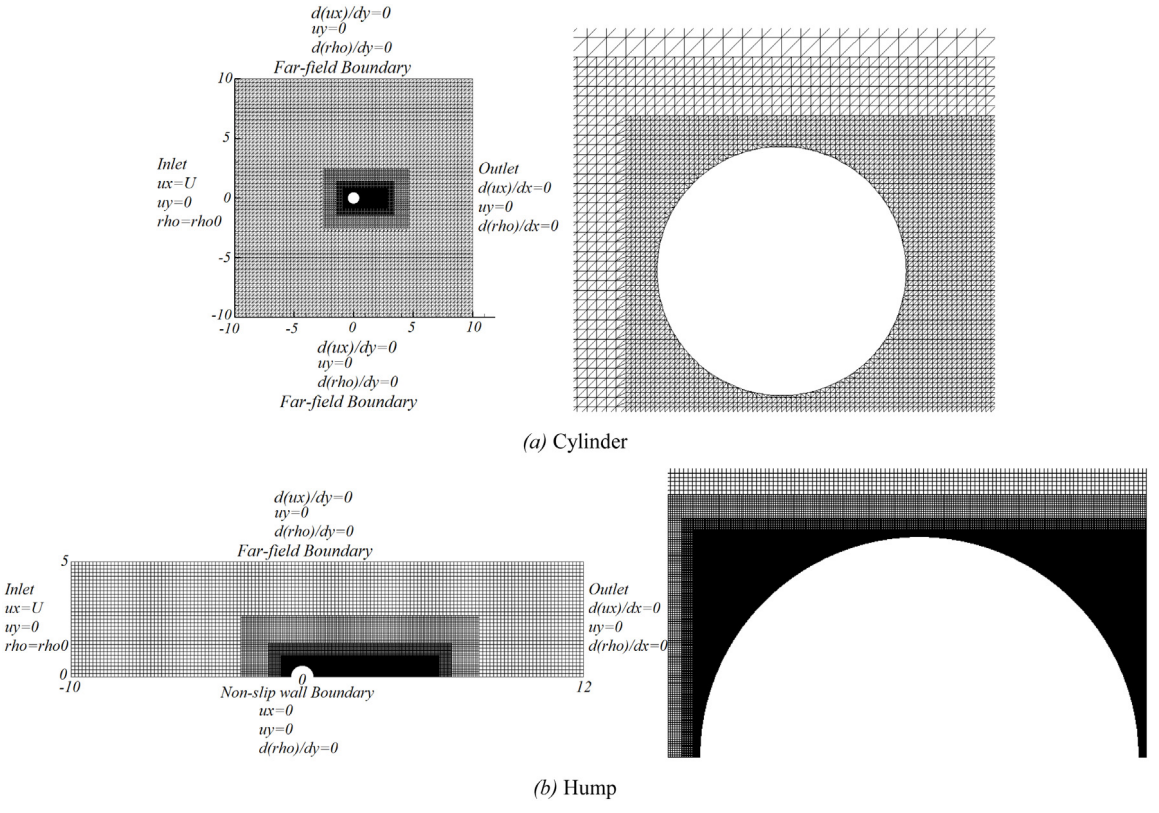

Fig. 3. Tree grid used for simulating the flow around these two particular geometries.

the following two essential equations are to be considered

$$Re = UL/\nu \tag{8}$$

$$\nu = (2\tau - 1)\Delta x^2/(6\Delta t) \tag{9}$$

Introducing Eq. (8) into Eq. (9), it is obtained

$$UL/Re = (2\tau - 1)\Delta x^2/(6\Delta t) \tag{10}$$

where U is the initial velocity and L is the characteristic length.

From Eq. (10) and considering the definition of the lattice non-dimensional velocity presented in Section 1.2, the value of the single relaxation time τ is given by, Eq. (11). Notice that the single relaxation time is initially introduced in Eq. (2).

$$\tau = 3UL/(Re\Delta x) + 0.5 \tag{11}$$

Empirically, when the relaxation time τ is close to 0.5, the stability of LBM is compromised. For numerical simulations involving high Reynolds numbers, the grid spacing Δx must be small enough to maintain the relaxation time well above 0.5. As a result, at high Reynolds numbers a mesh refinement is inevitable, although this will greatly increase the computational burden. This is the main reason why the original LBM cannot be directly applicable to numerical simulations at high Reynolds numbers. The MRT-LBM and LES-LBM approaches are used in the present manuscript as mathematical tools to numerically stabilize the conventional LBM at high Reynolds numbers, these mathematical tools are discussed and explained in the following sub-sections. According to the authors' knowledge, this is the first time the combination of tree grid technology with LES-LBM is being employed.

3.1. Multiple-relaxation-time lattice Boltzmann method

The main difference between the MRT-LBM approach [12–17] and the LBGK model, is that in the first approach, multiple relaxation time terms are used to construct an nth order vector, while on the second one a single relaxation

time term is required. The evolution equations of the MRT-LBM and the LBGK are shown respectively as

$$\begin{cases} f_\alpha(\vec{r}+e_\alpha\Delta t, t+\Delta t) - f_\alpha(\vec{r},t) = 1/\tau(f_\alpha^{eq}(\vec{r},\vec{\xi}) - f_\alpha(\vec{r},\vec{\xi},t)) & LBGK-Single \\ \vec{f}_\alpha(\vec{r}+e_\alpha\Delta t, t+\Delta t) - \vec{f}_\alpha(\vec{r},t) = \vec{\Lambda}_{\alpha\beta}[\vec{f}_\beta^{eq}(\vec{r},\vec{\xi}) - \vec{f}_\beta(\vec{r},\vec{\xi},t)] & LBM-MRT \end{cases} \tag{12}$$

where $\vec{f}_\alpha$ is a nine-order vector and $\vec{\Lambda}_{\alpha\beta}$ is a 9×9 collision diagonal matrix given by

$$\vec{\Lambda}_{\alpha\beta} = \begin{pmatrix} 1/\tau_1 & 0 & 0 & 0 & 0 & 0 & 0 & 0 & 0 \\ 0 & 1/\tau_2 & 0 & 0 & 0 & 0 & 0 & 0 & 0 \\ 0 & 0 & 1/\tau_3 & 0 & 0 & 0 & 0 & 0 & 0 \\ 0 & 0 & 0 & 1/\tau_4 & 0 & 0 & 0 & 0 & 0 \\ 0 & 0 & 0 & 0 & 1/\tau_5 & 0 & 0 & 0 & 0 \\ 0 & 0 & 0 & 0 & 0 & 1/\tau_6 & 0 & 0 & 0 \\ 0 & 0 & 0 & 0 & 0 & 0 & 1/\tau_7 & 0 & 0 \\ 0 & 0 & 0 & 0 & 0 & 0 & 0 & 1/\tau_8 & 0 \\ 0 & 0 & 0 & 0 & 0 & 0 & 0 & 0 & 1/\tau_9 \end{pmatrix} \tag{13}$$

Eq. (12) explains the evolution process of the distribution functions. Considering the MRT-LBM, the collision process is accomplished by the operation of matrices and vectors. The relation between the distribution functions vector and the moment vector $\vec{m}_\alpha$ is obtained from

$$\vec{m}_\alpha = \vec{M}_{\alpha\beta}\cdot\vec{f}_\beta; \quad \vec{f}_\alpha = \vec{M}_{\alpha\beta}^{-1}\cdot\vec{m}_\beta \tag{14}$$

where $\vec{M}_{\alpha\beta}$ is a 9×9 switch matrix and $\vec{f}_\alpha$ is the distribution functions vector. The collision process in MRT-LBM is defined by

$$\vec{f}'_\alpha = \vec{f}_\alpha - \vec{\Lambda}_{\alpha\beta}\left[\vec{f}_\beta - \vec{f}_\beta{}^{eq}\right] \tag{15}$$

$\vec{f}'_\alpha$ is the distribution functions vector after the collision step. Multiplying the switch matrix $\vec{M}_{\alpha\beta}$ on both sides of Eq. (15), it is obtained

$$\vec{m}'_\alpha = \vec{m}_\alpha - \vec{S}_{\alpha\beta}\left[\vec{m}_\beta - \vec{m}_\beta{}^{eq}\right] \tag{16}$$

where $\vec{m}_\alpha{}^{eq} = \vec{M}_{\alpha\beta}\cdot\vec{f}_\beta{}^{eq}$ is the vector of the equilibrium moment and $\vec{S}_{\alpha\beta} = \vec{M}_{\alpha\beta}\vec{\Lambda}_{\beta\alpha}\vec{M}_{\alpha\beta}^{-1} = diag(s_1, s_2, \ldots, s_n)$ is a diagonal matrix.

After the collision process, the collided distribution functions vector $\vec{f}'_\alpha = \vec{M}_{\alpha\beta}^{-1}\cdot\vec{m}'_\beta$ is obtained. The computational approach of the MRT-LBM is addressed as follows:

(1) Initializing the whole flow field with macroscopic quantities and computing the equilibrium distribution functions.
(2) Calculating the vector of velocity distribution functions $\vec{f}'_\alpha = \vec{M}_{\alpha\beta}^{-1}\cdot\vec{m}'_\beta$ and moment $\vec{m}_\alpha = \vec{M}_{\alpha\beta}\cdot\vec{f}_\beta$.
(3) Performing the evolution process, including collision step $\vec{f}'_\alpha = \vec{f}_\alpha - \vec{\Lambda}_{\alpha\beta}\vec{M}_{\alpha\beta}^{-1}\left[\vec{m}_\beta - \vec{m}_\beta^{eq}\right]$ and streaming step.
(4) Computing the macroscopic quantities and resetting the distribution functions on the boundaries.

3.2. Large-eddy-simulation lattice Boltzmann method

The large-eddy-simulation LBM [18–22,51] is another method to improve the numerical stability of the original lattice Boltzmann method. By using the Smagorinsky eddy viscosity model, the total kinematic viscosity equals the sum of the fluid kinematic viscosity ν and the eddy kinematic viscosity ν_t,

$$\nu_{total} = \nu + \nu_t \tag{17}$$

where $\nu_t = C\Delta_f^2\left|\overline{S}_{ij}\right|$ is the eddy kinematic viscosity. C is the constant coefficient of the Smagorinsky eddy viscosity model. Δ_f is the filter scale and $\left|\overline{S}_{ij}\right|$ is the magnitude of large scale strain rate tensor. According to reference [27], the total relaxation time can be obtained from Eq. (18)

$$\tau_{total} = 3(\nu + C\Delta_f^2\left|\overline{S}_{ij}\right|) + 0.5 \tag{18}$$

The non-equilibrium stress tensor, used to determine the large scale strain rate tensor, is given by $\overline{\Pi}_{i,j} = \sum e_{\alpha i}e_{\alpha j}(\overline{f}_\alpha - \overline{f}_\alpha^{eq})$. It is important to realize that whenever Eq. (18) is implemented in Eq. (3), the original LBGK model is transformed into LES-LBM. Notice that the collision operator used in the LES-LBM, defined as the right hand side term of Eq. (3), is essentially the same as the one used in the conventional LBM, the only difference is that the relaxation time term τ, used in conventional LBM, is replaced by τ_{total} in LES-LBM.

Please cite this article as: B. An, J.M. Bergadà, F. Mellibovsky et al., New applications of numerical simulation based on lattice Boltzmann method at high Reynolds numbers, Computers and Mathematics with Applications (2019), https://doi.org/10.1016/j.camwa.2019.10.002.

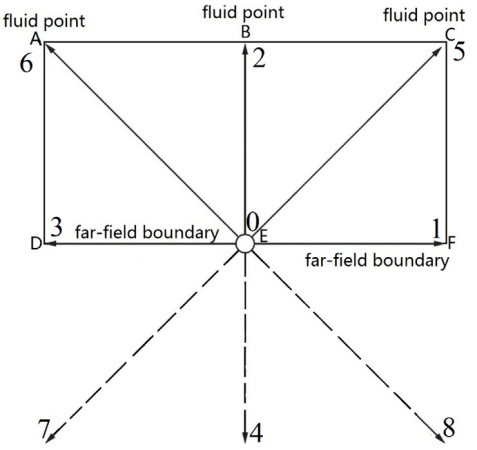

Fig. 4. Far-field boundary.

The computational steps to follow in order to implement the LES-LBM are addressed as follows:

(1) Initializing the whole flow field with macroscopic quantities and computing the equilibrium distribution functions.
(2) Filtering process, obtaining the processed macroscopic quantities $(\overline{\rho}, \overline{u})$.
(3) Computing the processed equilibrium distribution functions $\overline{f}^{eq}$, and $f = \overline{f}^{eq}$.
(4) Performing the evolution (collision and streaming) process.
(5) Computing macroscopic quantities and resetting the distribution functions on the boundaries.

4. Boundary conditions

4.1. Far-field, inlet and outlet boundary conditions

The non-equilibrium extrapolation scheme presented by Guo et al. [52] was employed to define the far-field boundary condition in the current numerical cases. The basic idea behind this scheme is that the distribution function of each direction can be classified into two parts, known as the non-equilibrium term and the equilibrium term.

As shown in Fig. 4, grid nodes ***A***, ***B*** and ***C*** are flow points, grid nodes ***D***, ***E*** and ***F*** are far-field boundary points. For the points ***E*** and ***B***. the distribution function of each direction is written as

$$f_\alpha(E,t) = f_\alpha^{eq}(E,t) + f_\alpha^{neq}(E,t) \tag{19}$$

$$f_\alpha(B,t) = f_\alpha^{eq}(B,t) + f_\alpha^{neq}(B,t) \tag{20}$$

The equilibrium part $f_\alpha^{eq}(E,t)$ is obtained from the macroscopic quantities of point ***E***. While, the non-equilibrium distribution functions of point ***E*** can be replaced by those of point ***B***.

$$f_\alpha^{neq}(E,t) \approx f_\alpha^{neq}(B,t) \tag{21}$$

Hence, the distribution functions of point ***E*** become

$$f_\alpha(E,t) = f_\alpha^{eq}(E,t) + f_\alpha(B,t) - f_\alpha^{eq}(B,t) \tag{22}$$

4.2. Wall boundary conditions

For the straight wall boundaries involved in all cases, the same non-equilibrium extrapolation scheme presented in reference [52] is used in the present paper. When considering the curved wall boundaries, there are several popular schemes [53–55] to be considered. In the present paper, all three schemes were tested when evaluating the flow around a hump and a cylinder. Based on the case of the flow around a cylinder at Reynolds number 100, and once evaluated the results presented in Section 5.1, Tables 1 and 3, it is concluded that the most appropriate scheme for the present applications was the one from Mei et al. [53]. This particular scheme is outlined next.

In Fig. 5, grid nodes ***a*** and ***c*** are fluid-domain points, grid node ***w*** belongs to wall boundary points and grid node ***b*** is a virtual internal wall point. Mei et al. [53], presented an accurate curved boundary treatment, according to their theory, taking point ***b*** for instance, the virtual distribution function, on direction 6 see Fig. 1, is constructed by linear interpolation of points ***b***, ***c*** and ***w***, and given by

$$f_6^v(\vec{r}_b,t) = (1-\chi)F_8(\vec{r}_c,t) + \chi f_8^{ev}(\vec{r}_b,t) + 2\omega_8\rho\frac{3}{c^2}\vec{e}_6\cdot\vec{u}_w \tag{23}$$

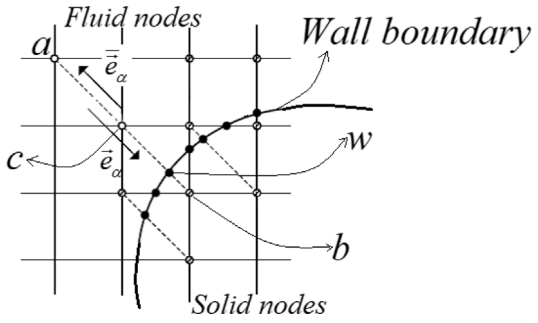

Fig. 5. Curved wall boundary.

Table 1
Comparison of the lift coefficient amplitude, drag coefficient mean value and Strouhal number obtained from the present paper with three different boundary schemes and several previous investigations at $Re = 100$.

Data source	Amplitude of *Cl*	Mean value of *Cd*	Strouhal number
Present work scheme [53]	±0.286	*1.39*	*0.164*
Present work scheme [54]	±0.32	*1.414*	*0.1643*
Present work scheme [55]	±0.265	*1.383*	*0.1646*
Ref. [29]	±0.287	*1.356*	*0.166*
Ref. [30]	–	*1.37*	*0.165*
Ref. [31]	±0.278	*1.352*	*0.161*
Ref. [32]	±0.287	–	–

where $\vec{u}_w$ is the non-dimensional velocity of the point $\boldsymbol{w}$, which is $\vec{0}$ in the present cases, and χ is the linear interpolation factor obtained by Eq. (25). The equilibrium virtual distribution function on direction 8 (see Fig. 1), is given by.

$$f_8^{ev}(\vec{r}_b, t) = \omega_8 \rho(\vec{r}_c, t)\left[1 + \frac{3}{c^2}\vec{e}_8 \cdot \vec{u}_b + \frac{9}{2c^4}(\vec{e}_8 \cdot \vec{u}_c)^2 - \frac{3}{2c^4}\vec{u}_c\vec{u}_c\right] \tag{24}$$

where $\vec{u}_c$ is the velocity of the point $\boldsymbol{c}$, and $\vec{u}_b$ is the unknown virtual velocity of the point $\boldsymbol{b}$. This velocity is presented in Eq. (25) as a function of the embedded depth Δ_e.

$$\begin{aligned} &\text{if } \Delta_e < 1/2 \Rightarrow \vec{u}_b = \vec{u}_c, \text{ and } \chi = \frac{2\Delta_e - 1}{\tau - 2} \\ &\text{if } \Delta_e \geq 1/2 \Rightarrow \vec{u}_b = \frac{\Delta_e - 1}{\Delta_e}\vec{u}_c + \frac{1}{\Delta_e}\vec{u}_w, \text{ and } \chi = \frac{2\Delta_e - 1}{\tau + 0.5} \end{aligned} \tag{25}$$

Substituting Eqs. (24) and (25) into Eq. (23) the virtual distribution function of point $\boldsymbol{b}$ is obtained. In this way, the streaming operation from point $\boldsymbol{b}$ to point $\boldsymbol{c}$ is smoothly achieved.

4.3. Virtual boundary condition

The virtual boundary condition is only considered when the tree grid is used in the numerical simulations. The process to construct the macroscopic quantities and the distribution functions in the virtual boundaries, is defined in this subsection. In this paper, none of the nodes in virtual boundaries were involved in the streaming process. The distribution functions of each node, were calculated by a set of new schemes developed by the present authors based on the initial concepts given in references [48–50]. After obtaining the macroscopic quantities, the distribution functions in the virtual boundaries, were calculated with the use of the non-equilibrium extrapolation scheme [52]. In order to construct the macroscopic terms in the virtual boundaries, there is a need to perform an interpolation process, using the macroscopic quantities on both sides of virtual boundaries. In the present paper, the grid spacing relation existing between both sides of the virtual boundaries, is given by

$$\Delta x_{coarse}/\Delta x_{fine} = 2 \tag{26}$$

From Eq. (26) and for a constant non-dimensional time step Δt, the lattice Boltzmann equation evolves only once on the coarse cell, while it evolves twice on the fine grid. Hence, the interpolation process outlined in the previous paragraph is actually a simultaneous space–time interpolation.

It can be seen from Fig. 6(a) that, point $\boldsymbol{A}$ is a coarse grid node, while point $\boldsymbol{B}$ is an overlapping point of coarse and fine boundaries, and point $\boldsymbol{C}$ is a fine grid node. Considering a half time step $0.5\Delta t$, the macroscopic quantities of the point $\boldsymbol{B}$ can be constructed as

$$\psi(B)^{t+0.5\Delta t} = (\psi(A)^{t+0.5\Delta t} + 2\psi(C)^{t+0.5\Delta t})/3 \tag{27}$$

Please cite this article as: B. An, J.M. Bergadà, F. Mellibovsky et al., New applications of numerical simulation based on lattice Boltzmann method at high Reynolds numbers, Computers and Mathematics with Applications (2019), https://doi.org/10.1016/j.camwa.2019.10.002.

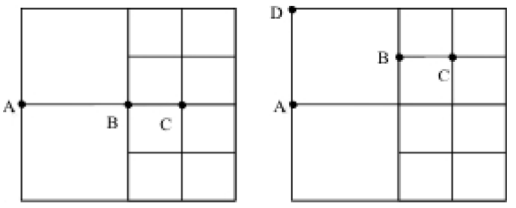

(a) (b)

Fig. 6. Virtual boundaries.

where ψ is the generic function of a macroscopic quantity, like velocity, density, pressure, etc. The time interpolation scheme at any given node, say node A, is evaluated according to the following equation.

$$\psi(A)^{t+0.5\Delta t} = 0.5(\psi(A)^{t} + \psi(A)^{t+\Delta t}) \tag{28}$$

In Fig. 6(b), points ***A*** and ***D*** are both coarse grid nodes, point ***C*** is a fine grid node and point ***B*** is a hanging point of virtual boundaries. The macroscopic quantities of the point ***B*** can be constructed as

$$\psi(B)^{t+0.5\Delta t} = (0.5\psi(A)^{t+0.5\Delta t} + 0.5\psi(D)^{t+0.5\Delta t} + 2\psi(C)^{t+0.5\Delta t})/3 \tag{29}$$

where the time interpolation scheme at points ***A*** and ***D*** follow the same pattern presented in Eq. (28).

It is to be realized that the macroscopic quantities at point ***B*** for both positions defined in Fig. 6(a) and (b), need to be determined at a half time step, $0.5\Delta t$, and after a full time step Δt. In order to obtain the macroscopic quantities at point ***B*** after a full time step, Eqs. (30) and (31) need to be respectively applied.

$$\psi(B)^{t+\Delta t} = (\psi(A)^{t+\Delta t} + 2\psi(C)^{t+\Delta t})/3 \tag{30}$$

$$\psi(B)^{t+\Delta t} = (0.5\psi(A)^{t+\Delta t} + 0.5\psi(D)^{t+\Delta t} + 2\psi(C)^{t+\Delta t})/3 \tag{31}$$

To sum up, from Eqs. (27) to (31), the macroscopic quantities of each grid node at different time steps on the virtual boundaries are obtained. Once the macroscopic quantities at each grid node and at different time steps have been obtained, the distribution functions of each node on the virtual boundaries, at different time steps, can be calculated through the non-equilibrium extrapolation scheme defined in Eq. (22).

5. Results and discussion

5.1. Application using tree grid technology in combination of LES-LBM

5.1.1. Flow over a circular cylinder

For all cases studied in the present paper, the upstream non-dimensional velocity was $U_\infty = 0.1$ and the initial non-dimensional fluid density was 1.0. As a first case to test the LES-LBM model based on the tree grid, the flow over a cylinder is considered. Initially, the three different schemes for curved boundaries introduced in Section 4.2 are evaluated at Reynolds number 100, and the results obtained are presented in Table 1. At this low Reynolds number the flow is periodic, therefore, the information presented in Table 1, was extracted once the simulation was fully converged, 15 s were run, and using a single oscillation cycle. Based on the results introduced in Table 1 and after comparing them with those reported in references [29–32], it was decided to employ the scheme from Mei et al. [52] for all curved boundaries studied in the present paper. Table 1 compares the lift coefficient amplitude, the average value of drag coefficient and the Strouhal number, obtained from the present simulation and several previous studies [29–32]. The agreement of all these parameters is very good.

In order to evaluate the efficiency of the tree grid over the standard Cartesian grid, Table 2 presents the computational time per time unit of the standard Cartesian grid (*T2*) and the tree grid (*T1*) at a steady Reynolds number 40, notice that the time ratio of *T2* over *T1* is 20.17. The first column of Table 2 defines the minimum grid spacing used in both meshes. The second column represents the total number of cells used for each mesh, and the third column characterizes the length ratio between the downstream steady bubble length and the cylinder diameter. It can be concluded from the table that, with the same minimum grid spacing, the standard Cartesian grid requires much longer computational time than the tree grid does, while still retaining an acceptable accuracy. For the present simulation, the computational time required is over 15 times smaller when employing the tree grid technology. It is the first time that LES-LBM model combined with the tree grid is proved much more efficient over the standard Cartesian grid. In reality, the tree grid technology is allowing to refine the mesh on the particular areas where the flow is having large momentum interchanges, therefore drastically reducing the total number of cells required.

In order to further assess the in-house code reliability, the flow for a turbulent Reynolds number, $Re = 3900$, was evaluated. The reason why laminar and turbulent Reynolds numbers were chosen, is to prove that the model proposed

Please cite this article as: B. An, J.M. Bergadà, F. Mellibovsky et al., New applications of numerical simulation based on lattice Boltzmann method at high Reynolds numbers, Computers and Mathematics with Applications (2019), https://doi.org/10.1016/j.camwa.2019.10.002.

Table 2
The ratio of computational time required between standard Cartesian grid (*SG*) and tree grid (*TG*) at $Re = 40$. *T2* characterizes the computational time per time unit whenever the standard Cartesian grid (*SG*) is used, and *T1* represents the same time when the tree grid (*TG*) is employed.

Grid spacing	*Total cells*		*Ls/L*	*Computational time per time unit*
$\Delta x = 0.009766$	*TG*	*16 652*	*4.4192*	$T1 = 0.00515625$ s
	SG	*1 042 792*	*4.4275*	$T2 = 0.104$ s

Table 3
Comparison of the drag coefficient mean value and Strouhal number obtained from the present paper and several previous investigations at $Re = 3900$.

Data source	Total number of cells	Strouhal number	Mean value of *Cd*
The present work $\Delta x = 0.009766$	*16 652*	*0.242*	*1.6*
The present work $\Delta x = 0.000305$	*3 567 008*	*0.2287*	*1.575*
Ref. [35]	*7 543 680*	*0.23*	*1.65*
Ref. [37]	*7 543 680*	*0.22*	*1.55*
Ref. [38]	*5 575 680*	*0.244*	*1.65*
Ref. [39]	–	*0.244*	
Ref. [40]	–	*0.243*	*1.749*
Ref. [41]	*871 200*	0.215 ± 0.005	*1.625*

is capable of producing good results under both conditions. Fig. 7(b) presents the vortex shedding process for a Reynolds number 3900. On each graph, the streamlines plots are presented on the left hand side alongside vorticity contour plots. Both plots are introduced at different time steps defined in Fig. 7(a). The same vortex evolution process was observed in the work done by Pereira et al. [39] Fig. 9 and Wang et al. [40] Fig. 8.

Table 3 introduces the Strouhal number and mean drag coefficient value obtained in the present simulation and when using two mesh densities. The result presented in Table 3, were obtained after the simulations were fully converged, over 50 s were simulated, a set of over 140 cycles lasting over ten seconds, were used to obtain the parameters defined Table 3. These values are compared with the 2D ones obtained in references [37,39–43]. It is observed that even for the largest grid spacing $\Delta x = 0.009766$, used in the present paper, and thanks to the use of the tree grid, the results obtained are very accurate.

Fig. 8 introduces the comparison between the temporal averaged pressure coefficient along the upper surface obtained in the present simulation and the ones obtained by four previous researches [33–36]. The agreement is very good, further enhancing the code reliability, proving as well that the new LES-LBM model coupled with tree grid is numerically stable for this Reynolds number.

5.1.2. Flow over a hump

Another typical bluff body configuration considered, to further evaluate the new LES-LBM coupled with tree grid, is the flow over a hump. Very interesting research has been undertaken on this configuration, see for example reference [28], yet according to the authors' knowledge no attempt to use LES-LBM based on tree grid to simulate flow over this particular bluff body has undertaken. One of the main advantages of using the proposed methodology, is that it allows to evaluate relatively large Reynolds numbers, well into the turbulent regime, and thanks to the use of the tree grid structure, considerable computational time reduction is obtained, see references [48–50]. Fig. 9 introduces the vortex shedding period divided in eight different time steps at Reynolds number 4000. It can be observed that, the vortices appear in a periodic cycle, attaching, detaching and streaming at different iteration steps. Regardless of the time step chosen, when comparing vortex shape and dimensions with reference [28] Fig. 10, the agreement is very good. Moreover, the Strouhal numbers obtained by the present simulation and Suzuki's work [28], were respectively 0.163 and 0.16. As a conclusion, it can be said the combination of the tree grid with the LES-LBM model at Reynolds number 4000, is producing very accurate results.

5.2. Applications of MRT-LBM

5.2.1. Lid driven cavity, case (a)

In this section, case (a) characterizing the lid driven cavity flow at Reynolds numbers varying from 2×10^4 to 1×10^6 was considered. The non-dimensional wall driven velocity was maintained at $U_{lid} = 0.1$. Fig. 10 introduces the numerical results obtained in the present paper, streamlines and vorticity contours are respectively presented on the left and right hand side of each figure. In the present paper as well as in reference [12], the MRT-LBM model was employed, the mesh density and boundary conditions were the same in both cases. The authors believe the small differences between figure 10

Please cite this article as: B. An, J.M. Bergadà, F. Mellibovsky et al., New applications of numerical simulation based on lattice Boltzmann method at high Reynolds numbers, Computers and Mathematics with Applications (2019), https://doi.org/10.1016/j.camwa.2019.10.002.

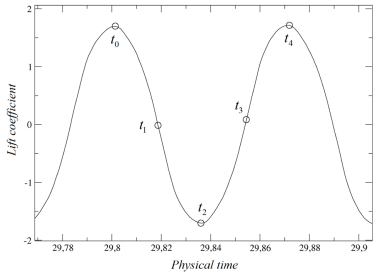

(a) Probes at different time steps

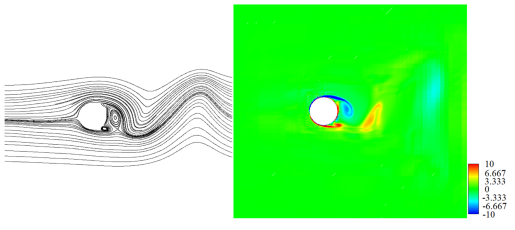

(b) $t_0 = 29.8014s$

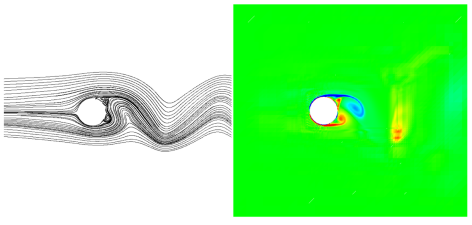

(c) $t_1 = 29.8187s$

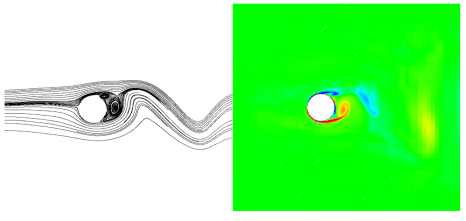

(d) $t_2 = 29.8361s$

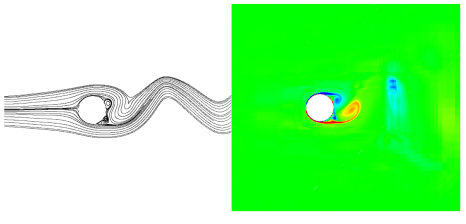

(e) $t_3 = 29.8545s$

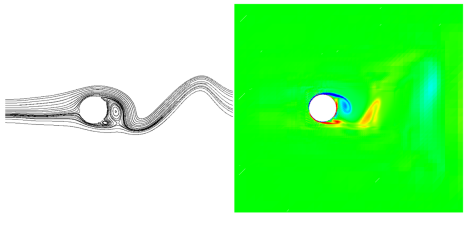

(f) $t_4 = 29.8719s$

Fig. 7. Comparison of streamlines between snapshots from the present paper at different time steps at Reynolds number 3900.

Please cite this article as: B. An, J.M. Bergadà, F. Mellibovsky et al., New applications of numerical simulation based on lattice Boltzmann method at high Reynolds numbers, Computers and Mathematics with Applications (2019), https://doi.org/10.1016/j.camwa.2019.10.002.

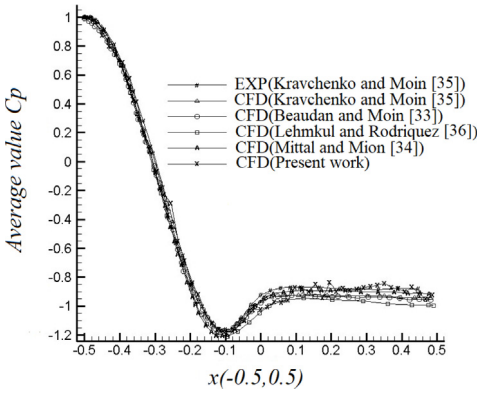

Fig. 8. Lift and drag coefficients on the cylinder, and mean pressure coefficient on the cylinder upper surface at Reynolds number 3900.

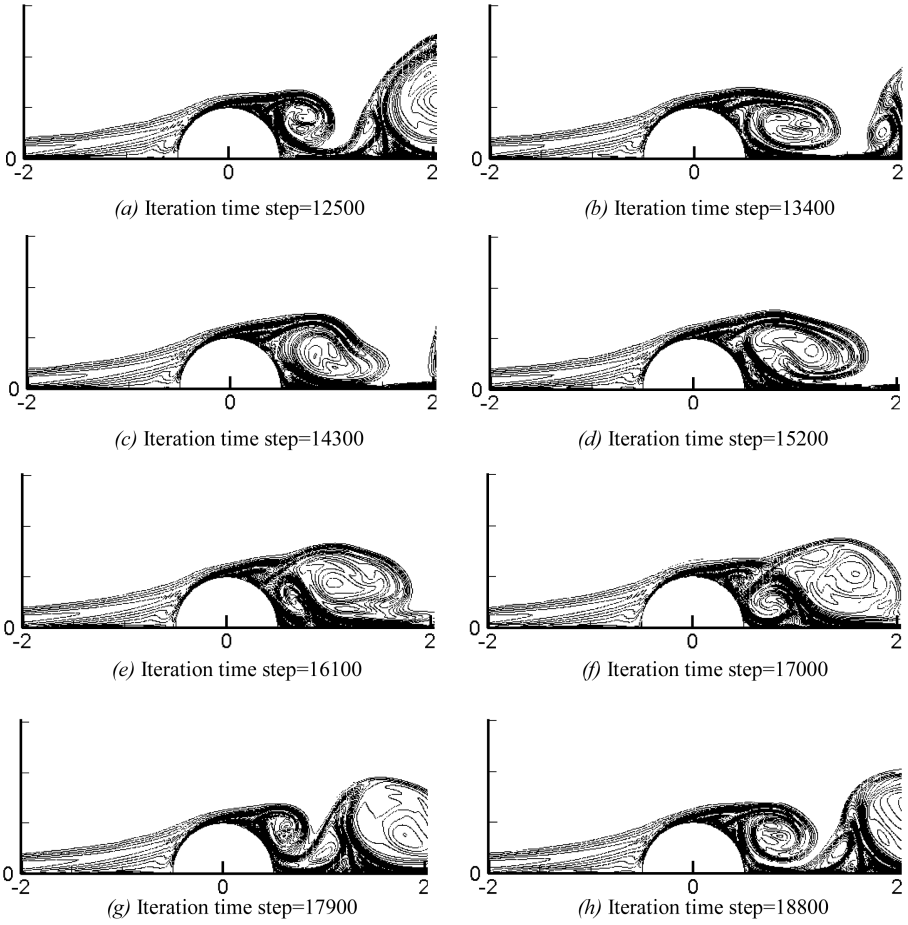

Fig. 9. Vortex shedding period divided in eight different time steps of the flow over a hump at Reynold number 4000.
Source: The figures presented here are comparable with those obtained by Suzuki [30].

and figure 1 in reference [12], are due to the instant each snapshot is taken, notice that the flow is turbulent and unsteady, and so it is time dependent. As can be seen from Fig. 10, the fluid unsteady behavior deteriorates as the Reynolds number increases. When the Reynolds numbers are relatively low, around 2×10^4 and 1×10^5, the flow instability is localized at some particular positions of the domain, namely the corners. On the contrary, the results at higher Reynolds numbers gradually show that the global instability appears throughout the cavity. For very high Reynolds numbers, $Re > 5 \times 10^5$, the flow configuration evolves in a highly random fashion, fluid motion is chaotic and no clear flow patterns can be

Please cite this article as: B. An, J.M. Bergadà, F. Mellibovsky et al., New applications of numerical simulation based on lattice Boltzmann method at high Reynolds numbers, Computers and Mathematics with Applications (2019), https://doi.org/10.1016/j.camwa.2019.10.002.

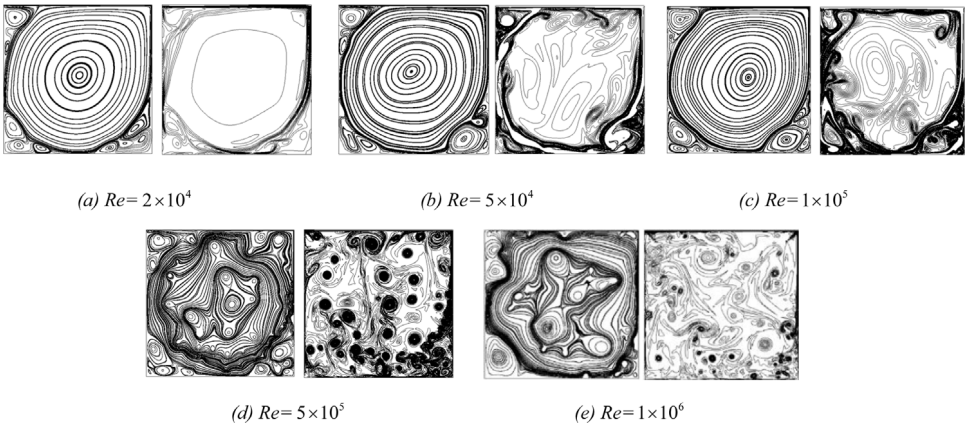

Fig. 10. Streamlines and vortex contours of the top wall driven velocity with different Reynolds numbers. Case (a) shows the numerical prediction obtained in this paper.

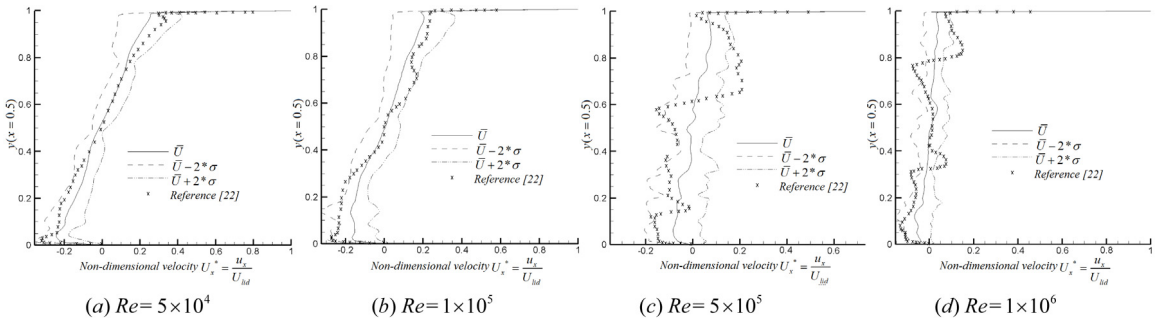

Fig. 11. U_x profiles along the vertical center lines at different Reynolds numbers.

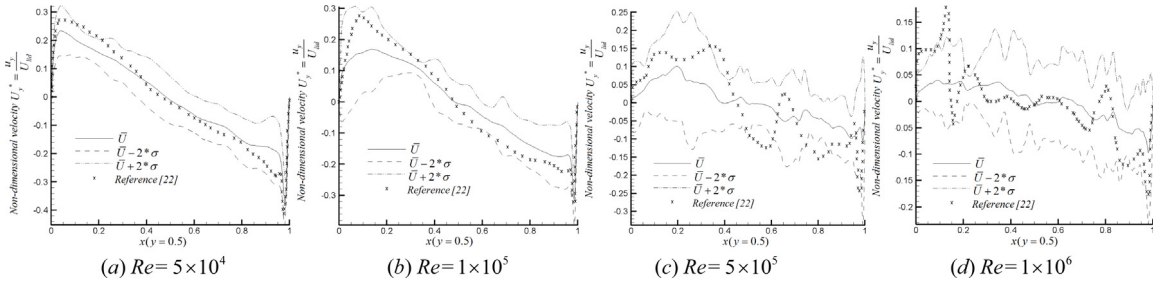

Fig. 12. U_y profiles along the horizontal center lines at different Reynolds numbers.

identified. This would explain why the flow structures obtained in the present paper are very similar to the ones obtained in reference [12] but not exactly the same. As a conclusion, it can be said that, the computational results obtained in this paper at Reynolds numbers lower than 1×10^5 show a good agreement with the data provided in reference [12]. Considering the chaotic flow time dependence typical at this regime, the agreement is quite acceptable. Notice that as Reynolds number increases, the turbulent motions become statistically isotropic, as established in the Kolmogorov's hypothesis of local isotropy.

In order to further evaluate the results obtained in the present simulation, Figs. 11 and 12 present the time-average non-dimensional velocity components U_x and U_y, respectively along the vertical and horizontal central lines at Reynolds numbers ranging from 2×10^4 to 1×10^6. The solid line represents the temporal average velocity components. The standard deviation σ is computed in the same figures and presented through enclosures formed by lines $\overline{U} + 2 * \sigma$ and $\overline{U} - 2 * \sigma$. Following the patterns presented in Fig. 10, it is seen that for $Re \leq 1 \times 10^5$, the respective U_x and U_y velocity distributions show a clear pattern characteristic of a forced vortex. Whenever $Re \geq 5 \times 10^5$, the time average velocity distributions still show the fluid is rotating clockwise. Figs. 11 and 12 also show that, the velocity gradient along the radial

Please cite this article as: B. An, J.M. Bergadà, F. Mellibovsky et al., New applications of numerical simulation based on lattice Boltzmann method at high Reynolds numbers, Computers and Mathematics with Applications (2019), https://doi.org/10.1016/j.camwa.2019.10.002.

Table 4
Time-averaged shear force and energy density of the lid-driven flow cavity at several Reynolds numbers.

Re	2×10^4	5×10^4	1×10^5	5×10^5	1×10^6
Skin friction coefficient	50.76556	20.33536	10.1937	4.0785	2.0422178
Energy density	13.41241	13.40949	13.40793	13.36985	13.36904

direction keeps decreasing with the Reynolds number increase, indicating the fluid is becoming fully chaotic. From these figures and considering the flow is highly turbulent, it is observed that the prediction presented in this paper has a good agreement with the results reported in reference [12], marked by symbols (×).

A few global values of the flow are reported in Table 4. The skin friction coefficient is defined as $C_f = |\tau_{lid}| / (0.5 \rho U_{lid}^2)$, where $\tau = \mu(du/dy) = \mu[(4 * u_{NY-1} - u_{NY-2} - 3 * u_{NY})/\Delta y]$, obtained through a second order accuracy scheme. The energy density is defined according to $E = \sum \left(\frac{1}{2}(U_x^2 + U_y^2)/N \times N\right)$, where the parameter N is the number of cells in any x or y directions. Notice that the friction force is generated due to the shear stresses acting on the lid. It is interesting to see that as the Reynolds increases, the skin friction coefficient on the lid tends to decrease. This performance seems to be the opposite than the one expected, but the results obtained can be understood when considering that the Reynolds number increase was achieved via reducing the fluid viscosity, not by increasing the lid velocity. Table 4 also presents the fluid kinetic energy density as a function of the Reynolds number. It can be observed that the energy density is pretty much constant regardless of the Reynolds number chosen, just a very small decrease is observed as Reynolds number increases. To understand such outcome, it needs to be remembered that the energy is transferred by the driven lid, and the lid velocity remains constant for all Reynolds numbers.

5.2.2. Two sided wall-driven cavity, top and bottom walls moving in opposite directions, case (b), at turbulent reynolds numbers

In this sub-section, the in-house new code will be used to study the two-sided wall-driven cavities at turbulent Reynolds numbers. Based on the authors' knowledge, this case under the proposed Reynolds numbers, has not been studied before. To perform this study, it was decided to use a very fine mesh, having a resolution of 2048 × 2048. The use of such resolution, allows a more accurate understanding of the chaotic behavior of the flow inside the cavity, as well as the visualization of the process followed by large-scale structures when breaking into smaller eddies. Notice that the y^+ after performing the simulation at the largest Reynolds number tested for case (b) was 0.34. Before presenting the new results, it is important to note that, during the present investigation and via using a rotational symmetry parameter as well as a mirror symmetry parameter, not presented in this paper, which evaluated the temporal U_x and U_y velocities from two probes located at $(x = L/2, y = L/4)$ and $(x = L/2, y = 3L/4)$, the authors observed the flow lose its symmetry at Reynolds number 2×10^4. Therefore, for cases (b) and (c) presented in this paper, the flow is chaotic, yet for the smallest Reynolds numbers presented in these cases, the flow still retains a quasi-symmetry.

Fig. 13 introduces at Reynolds numbers 3×10^4, 5×10^4, 2×10^5, 3×10^5 and 1×10^6, the new numerical results of the cavity flow with top and bottom walls moving in opposite directions. Each figure shows streamlines on the left hand side and the vorticity contours on the right. It can be observed that for Reynolds numbers smaller than or equal to 2×10^5, streamlines and even vorticity contours reveal a rotational quasi-symmetry. This rotational quasi-symmetry disappears at a Reynolds numbers higher than 2×10^5, due to the high vorticity embedded in the fluid. Notice that at Reynolds numbers 3×10^5 or higher, small positive and negative vortices appear that are randomly distributed across the fluid domain.

Regarding the vorticity associated to the fluid, it is realized that in all Figs. 13 and 16, the small scale vortices flourish as the Reynolds number increases. This small scale vorticity takes full control of the fluid movement whenever the Reynolds number is between 2×10^5 and 3×10^5 for cases (b) and (c), and based on the results presented in Fig. 10, the same happens between the Reynolds number 1×10^5 and 5×10^5 for case (a). These small scale eddies keep reducing in size as the Reynolds number increases, see Figs. 10, 13 and 16. Such effect is so overwhelming that for these very high Reynolds numbers, any sort of rotational quasi-symmetry completely vanishes. As a general trend it can be said that, a rise on the Reynolds number generates an increase of fluid vortex intensity.

Figs. 14 and 15 present the non-dimensional velocity profiles, U_x along the central y axis and U_y along the horizontal axis located at $y = 3L/4$. The standard deviation σ is introduced in the same figures, and presented through enclosures formed by lines $\overline{U} + 2 * \sigma$ and $\overline{U} - 2 * \sigma$. Notice that the rotational quasi-symmetry is observed, in Fig. 13, until the Reynolds number is around 2×10^5. At higher Reynolds numbers, there is an initial sudden drop of the fluid velocity nearby both walls, see Figs. 14 and 15(c), (d). The energy is almost instantaneously transferred from the moving walls to small scale vortices, and although there is a general flow circulation of the fluid around the cavity, see Fig. 13(d) and (e), the average non-dimensional velocities U_x and U_y, across the measuring y and x axes, are tending to zero, see Figs. 14 and 15(c), (d). All this indicates, that at very high Reynolds numbers, the fluid tends to lose its general turning speed and tends to be characterized by many small vortical structures randomly localized.

Please cite this article as: B. An, J.M. Bergadà, F. Mellibovsky et al., New applications of numerical simulation based on lattice Boltzmann method at high Reynolds numbers, Computers and Mathematics with Applications (2019), https://doi.org/10.1016/j.camwa.2019.10.002.

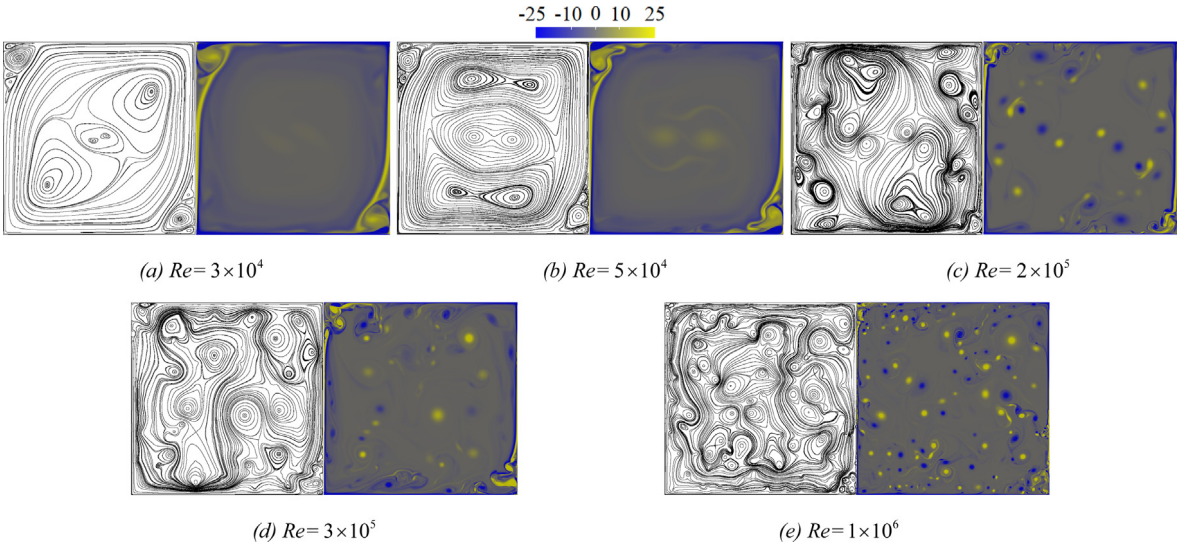

Fig. 13. Streamlines, left figures, and vorticity contours, right figures, generated when the top and bottom walls are driven towards opposite directions, case (b). Different Reynolds numbers were tested.

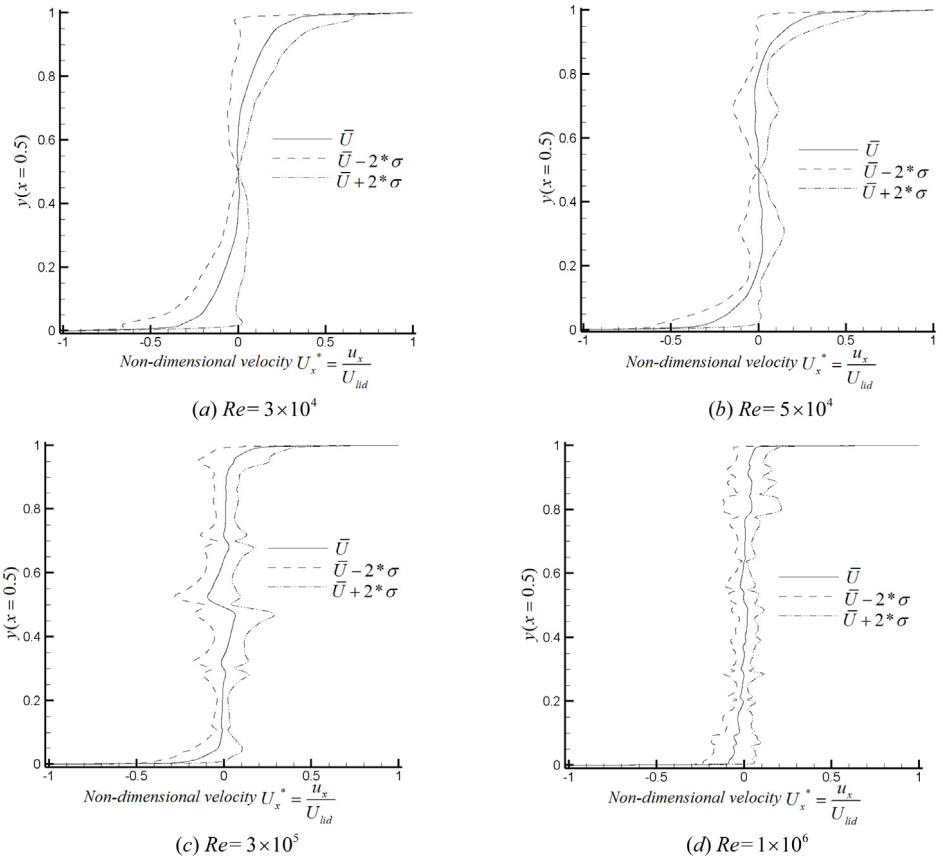

Fig. 14. U_x velocity profiles along the vertical center lines at different Reynolds numbers ($x = 0.5$).

Table 5 introduces the skin friction coefficient and energy density for case (b) as a function of the Reynolds number. The trend of these values is the same as the one provided in Table 4, the clarification of such trend was already established when introducing Table 4.

Please cite this article as: B. An, J.M. Bergadà, F. Mellibovsky et al., New applications of numerical simulation based on lattice Boltzmann method at high Reynolds numbers, Computers and Mathematics with Applications (2019), https://doi.org/10.1016/j.camwa.2019.10.002.

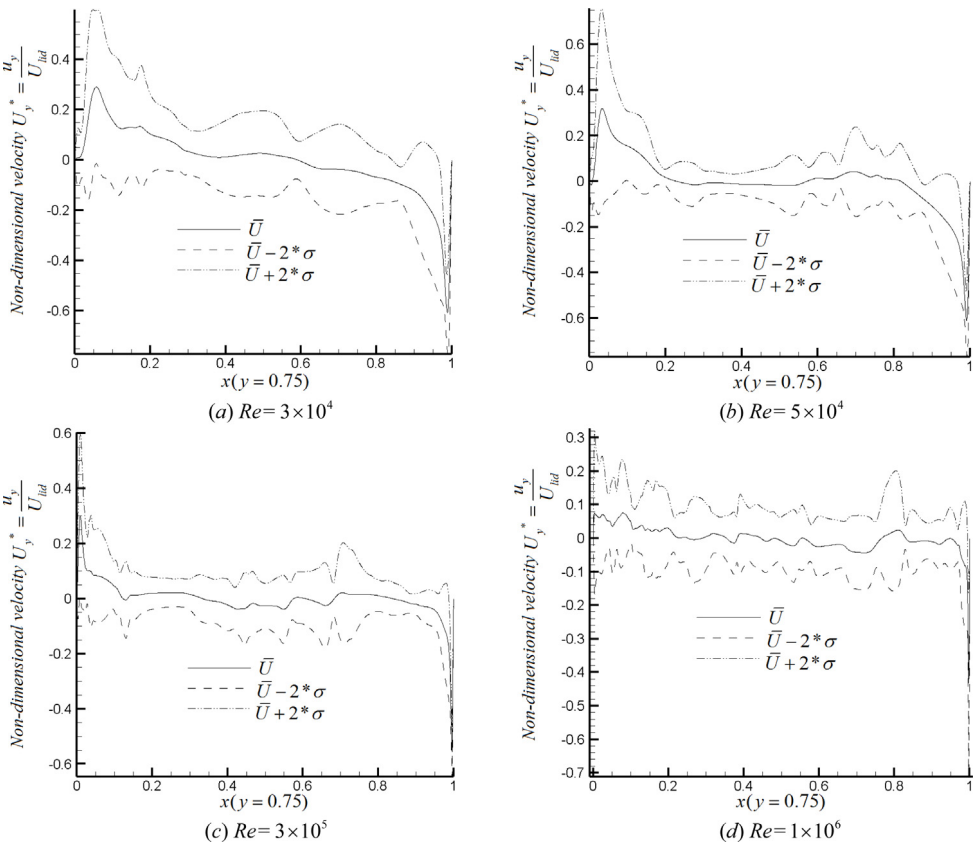

Fig. 15. U_y profiles along the horizontal center lines at different Reynolds numbers ($y = 0.75$).

Table 5
Time-averaged skin friction coefficient and energy density of the two-sided wall-driven cavity at several Reynolds numbers.

Re	2×10^4	3×10^4	4×10^4	5×10^4	1×10^5
Skin friction coefficient	40.8694	27.2178	20.3812	16.35406	8.1882
Energy density	13.3536	13.3532	13.3506	13.3503	13.348
Re	2×10^5	3×10^5	4×10^5	5×10^5	1×10^6
Skin friction coefficient	4.0692	2.72406	2.04326	1.63358	0.818
Energy density	13.346	13.3458	13.3456	13.34503	13.3446

Four videos, characterizing the flow dynamics at Reynolds numbers 3×10^4, 5×10^4, 4×10^5 and 1×10^6 are presented as supplementary materials (Appendix). The first video at Reynolds number 3×10^4, describes the vortex evolution inside the whole domain. It can be seen from it that, a huge primary vortex dominates the domain with few small scale secondary eddies around the top-left and bottom-right corners, both turning anti-clockwise. For this Reynolds number, the flow is rotational quasi-symmetric. The same characteristics can be observed at Reynolds number 5×10^4, the main difference resides in what can be observed in the center of the domain, then at this particular Reynolds number, four secondary structures can be seen turning anti-clockwise. Whenever the Reynolds number increases to 4×10^5, from the video it can be noticed that, the quasi-symmetry inherited from the steady solutions completely disappears. The domain is dominated by many secondary small scale eddies, since the primary topology no longer exists, the flow becomes fully chaotic. The same mechanism was discovered when Reynolds number reaches at 1×10^6, although the eddies are much smaller, indicating the flow is on an even higher level of randomness.

5.2.3. Two sided wall-driven cavity, top and bottom walls moving in the same direction, case (c), at turbulent reynolds numbers

The novel case (c) at turbulent Reynolds numbers from 3×10^4 to 1×10^6, is introduced in Fig. 16, where streamlines and vorticity contours are presented in each graph. The fluid flow pattern observed at Reynolds numbers smaller than or equal to 4×10^4, resembles what it is observed under laminar flow conditions, see reference [56]. Large upper and lower vortices

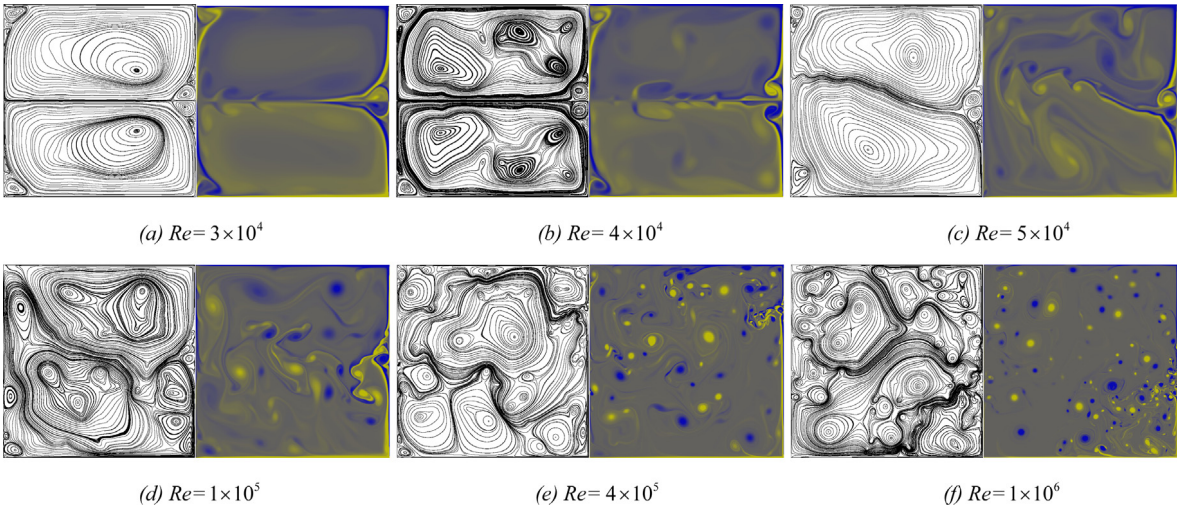

Fig. 16. Streamlines, left figures, and vorticity contours, right figures, when the top and bottom walls are driven towards the same direction. Different Reynolds numbers were tested.

turning in opposite directions, cover the entire domain. Nevertheless, as Reynolds number increases, small scale vortices start appearing around the two main vortices. The number of these small structures increases with Reynolds number, indicating that fluid inertial forces are taking over the bulk fluid motion. It is also interesting to realize that for Reynolds numbers smaller than 4×10^4, the vortical structures appearing on the fluid upper side have associated a negative sign, while the ones appearing on the fluid lower side are turning counter-clockwise. The mirror quasi-symmetry of the flow, appears to be existing until this particular Reynolds number. In fact, it was observed that the quasi-symmetry disappears at Reynolds numbers between 4×10^4 and 5×10^4. Whenever the Reynolds number is smaller than 1×10^5, the two main structures still dominate the fluid movement. At Reynolds number 1×10^5 the two main structures have completely disappeared, the flow becomes random and unpredictable, streamlines and vorticity contours are temporarily dependent, and the small positive and negative vortical structures are distributed randomly across the flow. Notice from Fig. 16(e) and (f), that as Reynolds number increases, the size of the vortical structures keep decreasing. The same observation can be made from Figs. 10 and 13(d), (e).

Figs. 17 and 18 present for several Reynolds numbers, the horizontal and vertical non-dimensional velocity profiles U_x and U_y along the vertical central line and horizontal line located at $y = 3L/4$ respectively. As already stated in the previous two cases, the velocity U_x profiles remain rather unaltered until reaching a Reynolds number between 4×10^4 and 5×10^4, following the trend expected under laminar conditions, see reference [56]. As already observed in case (b), at higher Reynolds numbers, the velocity changes abruptly nearby the walls, the average velocity U_x is pretty much constant along the y axis and having a value around zero. This abrupt change in velocity, is caused by the high kinetic energy transferred to the low viscosity fluid. Regarding the velocity profiles U_y along the horizontal axis, it is observed that regardless of the Reynolds number, the velocity distribution remains rather constant and having a value around zero. At Reynolds numbers below 5×10^4, the U_y velocity distribution increases the magnitude nearby the walls suddenly dropping to zero at the walls. For higher Reynolds numbers, no significant variations are found at any point. In fact, as the Reynolds number increases, just the standard deviation keeps suffering an increase, which characterizes the degree of randomness associated to the fluid. As Reynolds numbers overcome 4×10^5, the vorticity embedded in the fluid takes full control of the fluid motion and streamline patterns are very time-dependent, irregular and chaotic.

Following what was introduced in case (b), four videos, characterizing the flow dynamics at Reynolds numbers 3×10^4, 5×10^4, 4×10^5 and 1×10^6, and showing the flow evolution from quasi-symmetric to fully chaotic, are presented as supplementary materials (Appendix). The first movie introduces the dynamics of vorticity contour inside the enclosure at Reynolds number 3×10^4. The mirror quasi-symmetry was captured, which is similar on structure to the results at laminar Reynolds numbers. Large scale vortices dominate the domain, which is, in general, quite similar to what happened in case (b) at the same Reynolds number. At Reynolds number 5×10^4, from the video it can be outlined that, the mirror quasi-symmetry disappears, still, large scale primary structures dominate the domain. When Reynolds number increases to 4×10^5, the large scale vortices no longer exist, which are replaced by many small scale secondary eddies, revealing that the flow is already fully chaotic. The last movie is showing a similar degree of randomness, compared with the result of case (b) at the same Reynolds number.

As already introduced in cases (a) and (b), Table 6 presents the lid force and energy density for case (c). The trend of the parameters and its origin has already been explained in Tables 4 and 5.

Please cite this article as: B. An, J.M. Bergadà, F. Mellibovsky et al., New applications of numerical simulation based on lattice Boltzmann method at high Reynolds numbers, Computers and Mathematics with Applications (2019), https://doi.org/10.1016/j.camwa.2019.10.002.

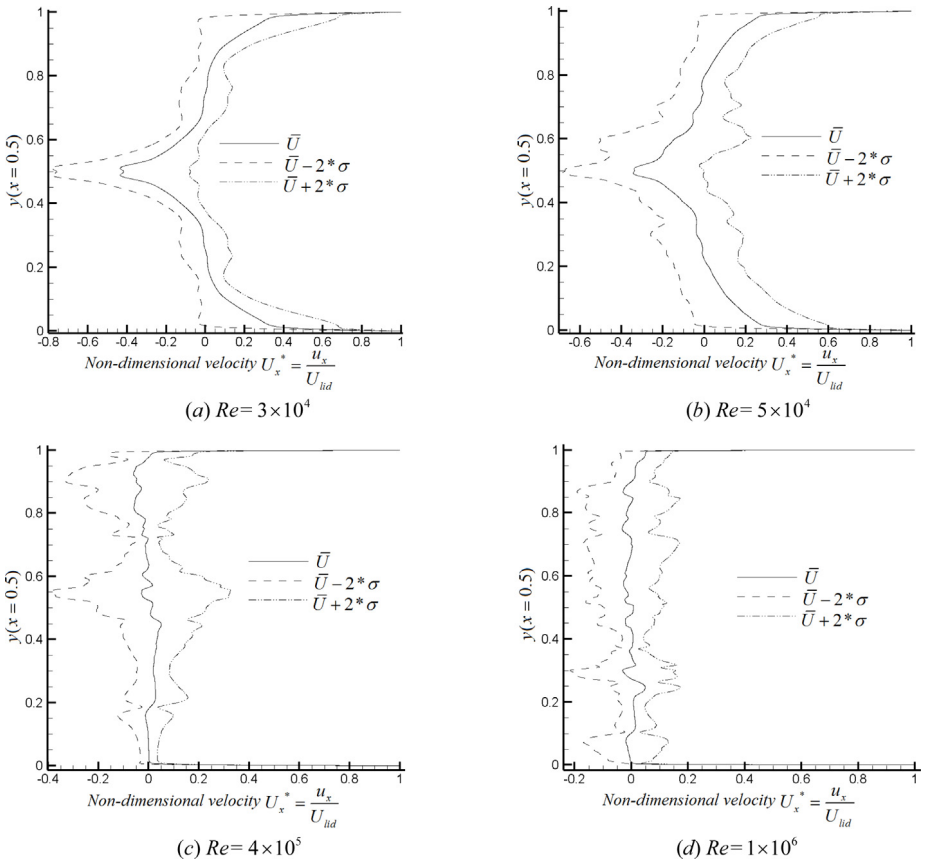

Fig. 17. U_x velocity profiles along the vertical center lines at different Reynolds numbers ($x = 0.5$).

Table 6
Time-averaged skin friction coefficient and energy density of the two-sided wall-driven cavity at several Reynolds numbers.

Re	2×10^4	3×10^4	4×10^4	5×10^4	1×10^5
Skin friction coefficient	40.8988	27.2698	20.45	16.35406	8.14668
Energy density	13.3567	13.3563	13.3548	13.3545	13.3495
Re	2×10^5	3×10^5	4×10^5	5×10^5	1×10^6
Skin friction coefficient	4.0749	2.7166	2.068	1.630214	0.814
Energy density	13.3483	13.3475	13.3467	13.34501	13.3447

Fig. 19 introduces the energy density and shear force for the new cases (b) and (c), information previously presented in Tables 5 and 6. It is observed that the energy density slightly decreases as Reynolds number increases. With the increase of Reynolds number, the large scale vortices break into tiny scale eddies, tending to reach the Kolmogorov scale vortices.

Four different energy levels are seen in Fig. 19(a) and Tables 5 and 6. The energy density associated to Reynolds numbers smaller than 3×10^4, is quite constant, notice that until this particular Reynolds number, the main vortical structures still exist. It is proved in the present paper, for both cases (b) and (c), that whenever the Reynolds number is between 3×10^4 and 1×10^5, the energy density drops fast. In this range of Reynolds number, the size of the vortical structures keep decreasing with the Reynolds number increase, and the large vortical structures progressively disappear. Whenever the Reynolds number is between 1×10^5 and 5×10^5, the flow is fully chaotic, vortical structures randomly appear across the fluid domain, and the size of these vortical structures decrease with the Reynolds number increase. At Reynolds numbers ranging from 5×10^5 to 1×10^6, the randomly localized vortical structures are already very tiny, and despite the fact that such structures keep reducing its size as the Reynolds number increases, there is a negligible modification of the vortices dimensions. Looking at Fig. 19(b), which is presenting the skin friction coefficient evaluated on the top lid, it is observed a similar trend than the one shown in Fig. 19(a). For all cases, the wall-driven velocity is 0.1,

Please cite this article as: B. An, J.M. Bergadà, F. Mellibovsky et al., New applications of numerical simulation based on lattice Boltzmann method at high Reynolds numbers, Computers and Mathematics with Applications (2019), https://doi.org/10.1016/j.camwa.2019.10.002.

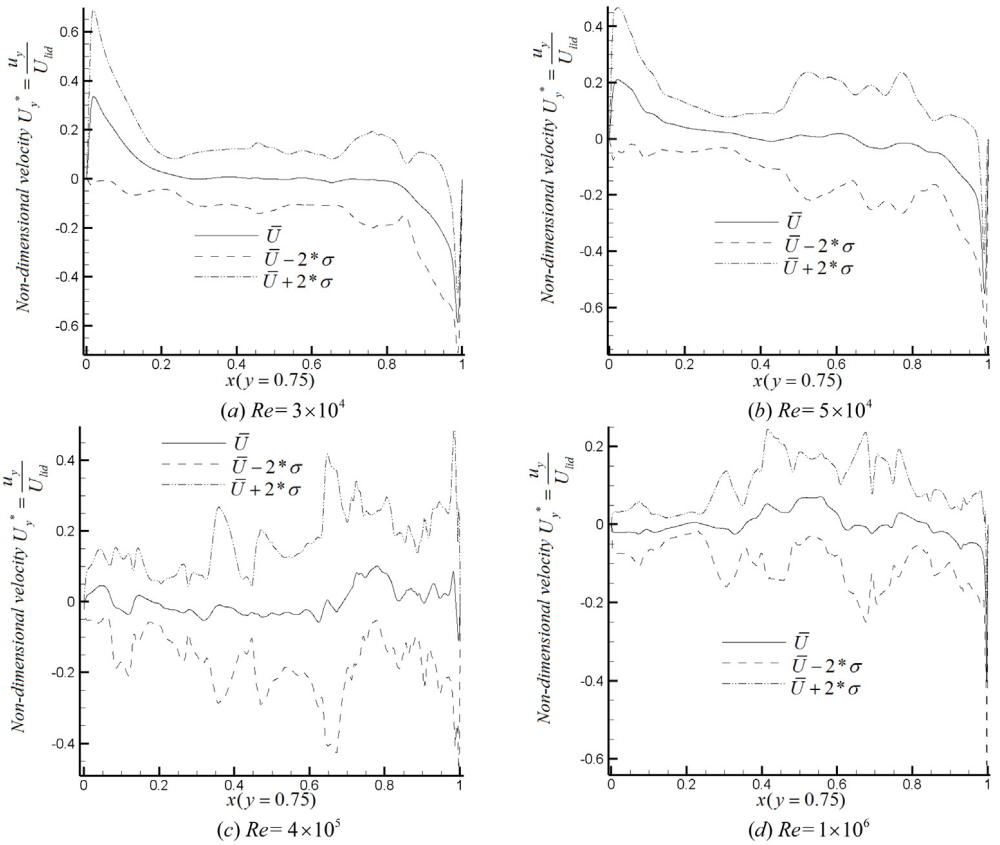

Fig. 18. U_y profiles along the horizontal center lines at different Reynolds numbers ($y = 0.75$).

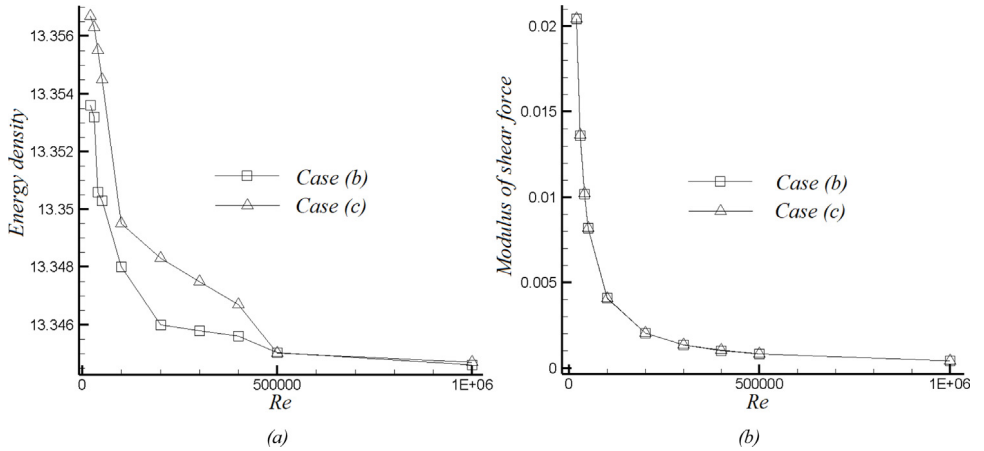

Fig. 19. Energy density and shear force versus Reynolds number for both cases (b) and (c).

which is constant for all tested Reynolds numbers, as a result, the viscosity has to be decreased in order to increase the Reynolds number, therefore, explaining the modulus of the shear force decrease.

In order to further understand the energy associated to the different vortical structures, for two given Reynolds numbers 1×10^6 and 2×10^4, case (b), it is obtained the spectral decomposition from the temporary u_x obtained from a probe located at $(x = L/4, y = L/4)$. It is very interesting to observe that in the inertial subrange, the energy decays with a slope very close to $-5/3$. We can conclude that the MRT-LBM with the grid resolution 2048×2048, is capable of properly evaluating the energy cascade, although as can be seen in Figs. 20(a) and 21(a), the mesh is not dense enough to evaluate the dissipation range, Kolmogorov scales.

Please cite this article as: B. An, J.M. Bergadà, F. Mellibovsky et al., New applications of numerical simulation based on lattice Boltzmann method at high Reynolds numbers, Computers and Mathematics with Applications (2019), https://doi.org/10.1016/j.camwa.2019.10.002.

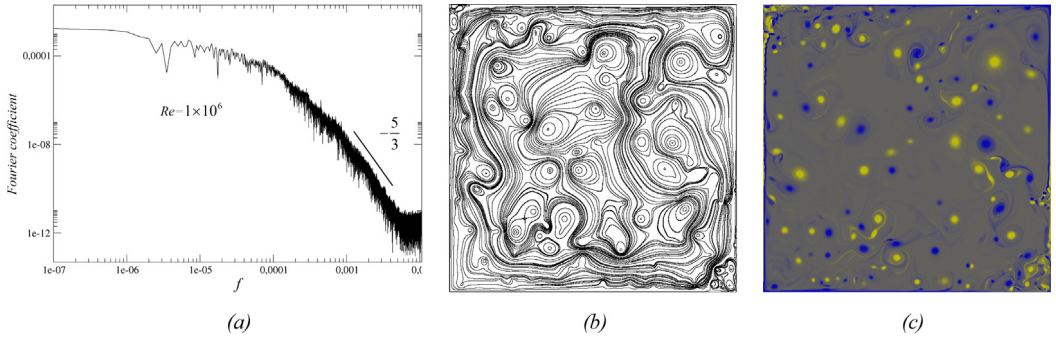

Fig. 20. (a) Spectral decomposition, (b) streamlines and (c) vorticity contours at Reynolds number 1×10^6 for case (b).

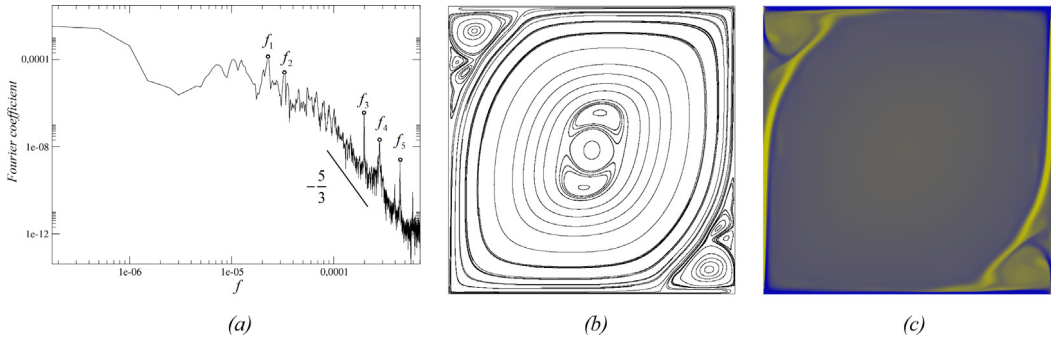

Fig. 21. (a) Spectral decomposition, (b) streamlines and (c) vorticity contours at Reynolds number 2×10^4 for case (b).

Regarding the spectral decomposition presented in Fig. 20(a), $Re = 1 \times 10^6$, it cannot be seen any particular relevant frequency peaks associated to the flow vortical structures. This fact is being understood when observing Fig. 20(b) and (c), which represent the streamlines and vorticity contours respectively. The entire flow domain is covered by small scale eddies, turning clockwise and anti-clockwise and transferring energy to smaller ones, it cannot be seen any vortical structure which is much bigger than the rest. The flow is homogeneous and isotropic, being these the characteristics of fully chaotic flow.

Fig. 21 presents the spectral decomposition, streamlines and vorticity contours of case (b) at $\mathrm{Re} = 2 \times 10^4$. At this particular Reynolds number, the flow is chaotic and quasi-symmetric. When looking at the spectral decomposition, it can be observed several relevant frequency peaks, defined as f_1 to f_5. The smallest frequency f_1, represents the energy associated to mean flow, main central vortex. The second frequency f_2, characterizes the vortices located in the center of the cavity, the very neat frequency f_3 is associated to the largest vortices located on the opposite corners. The last two frequencies f_4 and f_5 are connected to the pair of smaller vortices located as well on the opposite corners. As a conclusion that can be said that, the largest vortices contain the higher level of energy, as the vortices decrease in scale, their energy associated decreases and their frequency increases.

6. Conclusions

- A new code implementation, is introduced to combine the tree grid technology with the LES-LBM model, and it was used to evaluate the flow over several obstacles. The use of tree grid reduces the total number of cells employed in a given simulation, thus, reducing the time required for the simulations. The hardware requirements are also, reduced to a minimum when employing tree grid technology. This new code implementation is opening a door for the LBM CFD tool to be widely applied in many complex geometries. Making as well the application of LBM in three dimensional simulations, computationally less expensive.
- A set of new schemes, were generated to obtain the macroscopic quantities in the virtual boundaries between two different grid levels. The novel virtual boundary condition considers the mesh density on both sides of the boundary and the streaming time required for a fluid particle on each side of the mesh boundary.
- It is proved that, without the need of using body-fitted meshes, the LES-LBM model using tree grid technology generates, for the present cases, very accurate results.
- In the present study, using MRT-LBM in two-sided wall-driven cavities, top and bottom lids moving in the same direction or in opposite directions, were for the first time investigated under turbulent conditions, the Reynolds number range was between 2×10^4 and 1×10^6.

Please cite this article as: B. An, J.M. Bergadà, F. Mellibovsky et al., New applications of numerical simulation based on lattice Boltzmann method at high Reynolds numbers, Computers and Mathematics with Applications (2019), https://doi.org/10.1016/j.camwa.2019.10.002.

- For case (b), it was obtained that the flow quasi-symmetry remained until a Reynolds number 2×10^5. Small scale positive and negative randomly located vortices, start appearing for a Reynolds number between 2×10^5 and 3×10^5.
- For case (c), the flow quasi-symmetry disappeared for a Reynold number between 4×10^4 and 5×10^4. The appearance of randomly located positive and negative vortices, was observed for a Reynolds number around 1×10^5.
- Three very popular schemes employed in curved boundary conditions were tested in the present manuscript. The scheme producing more accurate results, was used in the present applications.

Acknowledgments

The authors would like to acknowledge the financial support from China Scholarship Council (CSC), from which, the first author received a four-year scholarship as a PhD scholar. The present paper presents part of the results obtained thanks to a competitive research project number FIS0016-77849-R founded by Spanish economy ministry.

Appendix A. Supplementary data

Supplementary material related to this article can be found online at https://doi.org/10.1016/j.camwa.2019.10.002. A total of eight videos are provided in this paper. Four videos characterizing case (b) at Reynolds numbers 3×10^4, 5×10^4, 4×10^5 and 1×10^6, are used to define the evolution of the fluid from the quasi-symmetric to the fully chaotic stages. Another four videos, define the same fluid evolution for case (c) at the same Reynolds numbers.

References

[1] G.R. McNamara, G. Zanetti, Use of the Boltzmann equation to simulate lattice automata, Phys. Rev. Lett. 61 (20) (1998) 2332–2335, http://dx.doi.org/10.1103/PhysRevLett.61.2332.
[2] S. Succi, Lattice Boltzmann Equation for Fluid Dynamics and Beyond, Clarendon Press, Oxford, 2001.
[3] Y.L. He, Y. Wang, Q. Li, Lattice Boltzmann Method: Theory and Applications, Science Press, Beijing, 2008.
[4] Z.H. Chai, B.C. Shi, A novel lattice Boltzmann model for the Poisson equation, Appl. Math. Model. 32 (2008) 2050–2058, http://dx.doi.org/10.1016/j.apm.2007.06.033.
[5] B. An, J.M. Bergada, A 8-neighbor model lattice Boltzmann method applied to mathematical-physical equations, Appl. Math. Model. 42 (2017) 363–381, http://dx.doi.org/10.1016/j.apm.2016.10.016.
[6] X.Y. He, S.Y. Chen, G.D. Doolen, A novel thermal model for the lattice Boltzmann method in incompressible limit, J. Comput. Phys. 146 (1) (1998) 282–300, http://dx.doi.org/10.1006/jcph.1998.6057.
[7] L. Deng, Y. Zhang, Y.W. Wen, B. Shan, H.M. Zhou, A fractional-step thermal lattice Boltzmann model for high peclet number flow, Comput. Math. Appl. 70 (5) (2015) 1152–1161, http://dx.doi.org/10.1016/j.camwa.2015.07.006.
[8] O. Filippova, D. Hänel, Lattice-BGK model for low Mach number Combustion, Internat. J. Modern Phys. C 9 (1998) 8, http://dx.doi.org/10.1142/S0129183198001308.
[9] M. Ashna, M.H. Rahimian, A. Fakhari, Extended lattice Boltzmann scheme for droplet combustion, Phys. Rev. E 95 (5) (2017) 053301, http://dx.doi.org/10.1103/PhysRevE.95.053301.
[10] S. Chen, G.D. Doolen, Lattice Boltzmann method for fluid flows, Annu. Rev. Fluid Mech. 30 (1) (1998) 329–364, http://dx.doi.org/10.1146/annurev.fluid.30.1.329.
[11] Y.H. Qian, D. dHumières, P. Lallemand, Lattice BGK models for Navier–Stokes equation, Europhys. Lett. 17 (6) (1992) 479–484, http://dx.doi.org/10.1209/0295-5075/17/6/001.
[12] Z.H. Chai, B.C. Shi, L. Zheng, Simulating high Reynolds number flow in two-dimensional lid-driven cavity by multi-relaxation-time lattice Boltzmann method, Chin. Phys. 15 (2006) 8, http://dx.doi.org/10.1088/1009-1963/15/8/038.
[13] D.A. Perumal, A.K. Dass, Simulation of incompressible flows in two-sided lid-driven square cavities. Part II-LBM, CFD Lett. 2 (1) (2010) 25–38.
[14] J.H. Lu, H.F. Han, B.C. Shi, Z.L. Guo, Immersed boundary lattice Boltzmann model based on multiple relaxation times, Phys. Rev. E 85 (2012) 016711, http://dx.doi.org/10.1103/PhysRevE.85.016711.
[15] A. Fakhari, T. Lee, Multiple-relaxation-time lattice Boltzmann method for immiscible fluids at high Reynolds numbers, Phys. Rev. E 87 (2013) 023304, http://dx.doi.org/10.1103/PhysRevE.87.023304.
[16] P. Lallemand, L.S. Luo, Theory of the lattice Boltzmann method: Dispersion, dissipation, isotropy, Galilean invariance, and stability, Phys. Rev. E 61 (2000) 6546, http://dx.doi.org/10.1103/PhysRevE.61.6546.
[17] K. Suga, Y. Kuwata, K. Takashima, A D3Q27 multiple-relaxation-time lattice Boltzmann method for turbulent flows, Comput. Math. Appl. 69 (2015) 518–529, http://dx.doi.org/10.1016/j.camwa.2015.01.010.
[18] S. Hou, J. Sterling, S. Chen, G.D. Doolen, A Lattice Boltzmann Subgrid Model for High Reynolds Number Flows, Pattern Formation and Lattice Gas Automata. Fields Institute Communications.
[19] M. Guo, X.L. Tang, Y.W. Su, X.Q. Li, F.J. Wang, Applications of three-dimensional LBM-LES combined model for pump intakes, Commun. Comput. Phys. 24 (1) (2018) 104–122, http://dx.doi.org/10.4208/cicp.OA-2017-0092.
[20] H.D. Yu, S.S. Girimaji, L.S. Luo, DNS and LES of decaying isotropic turbulence with and without frame rotation using lattice Boltzmann method, J. Comput. Phys. 209 (2) (2005) 599–616, http://dx.doi.org/10.1016/j.jcp.2005.03.022.
[21] Y.H. Dong, P. Sagaut, S. Marie, Inertial consistent subgrid model for large-eddy simulation based on the lattice Boltzmann method, Phys. Fluids 20 (2008) 035104, http://dx.doi.org/10.1063/1.2842379.
[22] S. Chen, A large-eddy-based lattice Boltzmann model for turbulent flow simulation, Appl. Math. Comput. 215 (2) (2009) 591–598, http://dx.doi.org/10.1016/j.amc.2009.05.040.
[23] A.C. Benim, E. Aslan, I. Taymaz, Investigation into LBM analysis of incompressible laminar flows at high reynolds numbers, WSEAS Trans. Fluid Mech. 4 (4) (2009).
[24] S. Ansumali, I.V. Karlin, Entropy function approach to the lattice Boltzmann method, J. Stat. Phys. 107 (1) (2002) 291–308, http://dx.doi.org/10.1023/A:1014575024265.
[25] F. Bösch, S.S. Chikatamarla, I.V. Karlin, Entropic multirelaxation lattice Boltzmann models for turbulent flows, Phys. Rev. E 92 (4) (2015) 043309, http://dx.doi.org/10.1103/PhysRevE.92.043309.

[26] R.Y. Zhang, X.W. Shan, H.D. Chen, Efficient kinetic method for fluid simulation beyond the Navier–Stokes equation, Phys. Rev. E 74 (4) (2006) 046703, http://dx.doi.org/10.1103/PhysRevE.74.046703.
[27] A. Montessori, G. Falcucci, P. Prestininzi, M. la Rocca, S. Succi, Regularized lattice Bhatnagar-Gross-Krook model for two-and three-dimensional cavity flow simulations, Phys. Rev. E 89 (5) (2014) 053317, http://dx.doi.org/10.1103/PhysRevE.89.053317.
[28] T. Suzuki, Effects of a synthetic jet acting on a separated flow over a hump, J. Fluid Mech. 547 (2006) 331–359, http://dx.doi.org/10.1017/S0022112005007366.
[29] H. Ding, C. Shu, K.S. Yeo, D. Xu, Numerical simulation of flows around two circular cylinders by mesh-free least square-based finite difference methods, Internat. J. Numer. Methods Fluids 53 (2) (2007) 305–332, http://dx.doi.org/10.1002/fld.1281.
[30] J.R. Meneghini, F. Saltara, C.L.R. Siqueira, J.A. Ferrari JR, Numerical simulation of flow interference between two circular cylinders in tandem and side-by-side arrangements, J. Fluids Struct. 15 (2) (2001) 327–350, http://dx.doi.org/10.1006/jfls.2000.0343.
[31] A.B. Harichandan, A. Roy, Numerical investigation of low Reynolds number flow past two and three circular cylinders using unstructured grid CFR scheme, Int. J. Heat Fluid Flow 31 (2) (2010) 154–171, http://dx.doi.org/10.1016/j.ijheatfluidflow.2010.01.007.
[32] S. Behara, S. Mittal, Flow past a circular cylinder at low Reynolds number: Oblique vortex shedding, Phys. Fluids 22 (5) (2010) 054102, http://dx.doi.org/10.1063/1.3410925.
[33] P. Beaudan, P. Moin, Numerical Experiments on the Flow Past a Circular Cylinder at Sub-Critical Reynolds Number (Ph.D. Thesis), Stanford University, 1995.
[34] R. Mittal, P. Moin, Suitability of upwind-biased finite difference schemes for large-eddy simulation of turbulent flows, AIAA J. 35 (8) (1997) 1415–1417, http://dx.doi.org/10.2514/2.253.
[35] G. Kravchenko, P. Moin, Numerical studies of flow over a circular cylinder at Re_D=3900, Phys. Fluids 12 (2) (2000) 403, http://dx.doi.org/10.1063/1.870318.
[36] O. Lehmkuhl, I. Rodriguez, R. Borrell, A. Oliva, Low-frequency unsteadiness in the vortex formation region of a circular cylinder, Phys. Fluids 25 (8) (2013) 085109, http://dx.doi.org/10.1063/1.4818641.
[37] D. You, P. Moin, A dynamic global-coefficient subgrid-scale eddy-viscosity model for large eddy simulation in complex geometries, Phys. Fluids 19 (6) (2007) 065110, http://dx.doi.org/10.1063/1.2739419.
[38] B.N. Rajani, A. Kandasamy, S. Majumdar, LES of flow past circular cylinder at Re =3900, J. Appl. Fluid Mech. 9 (3) (2016) 1421–1435, http://dx.doi.org/10.18869/acadpub.jam.68.228.24178.
[39] F.S. Pereira, G. Vaz, L. Eça, A comparison between rans and hybrid turbulence models for a low reynolds number, in: ASME 2015 34th International Conference on Ocean, Offshore and Arctic Engineering, 2015, OMAE2015-41235, V002T08A006.
[40] D.G. Wang, B. Hu, Q.X. Shui, Large eddy simulation combined with characteristic-based operator-split finite element method, Comput. Model. Eng. Sci. 107 (4) (2015) 297–320, http://dx.doi.org/10.3880/j.issn.1006-7647.2017.02.005.
[41] M. Breuer, Numerical and modeling influence on large eddy simulations for the flow past a circular cylinder, J. Heat Fluid Flow 19 (5) (1998) 512–521, http://dx.doi.org/10.1016/S0142-727X(98)10015-2.
[42] P.L. Bhatnagar, E.P. Gross, M. Krook, A model for collision processes in gases. I. Small amplitude processes in charged and neutral one-component systems, Phys. Rev. 94 (3) (1954) 511–525, http://dx.doi.org/10.1103/PhysRev.94.511.
[43] H.D. Chen, S.Y. Chen, W.H. Matthaeus, Recovery of the Navier–Stokes equations using a lattice-gas Boltzmann method, Phys. Rev. A 45 (8) (1992) R5339, http://dx.doi.org/10.1103/PhysRevA.45.R5359.
[44] A.J.C. Ladd, Numerical simulations of particulate suspensions via a discretized Boltzmann equation. Part I. Theoretical foundation, J. Fluid Mech. 271 (1994) 285–309, http://dx.doi.org/10.1017/S0022112094001771.
[45] Z.L. Guo, C.G. Zheng, Theory and Applications of Lattice Boltzmann Method, Science Press, Beijing, 2008.
[46] W.M. Sang, Numerical Simulation of Euler/N-S Equation Based on the Self-Adaptive Cartesian Grid (PhD. Dissertation), School of aeronautics, Northwestern Polytechnical University, Xi'an, 2002.
[47] W.M. Sang, F.W. Li, Numerical analysis of flows around 3-D high-lift system by adaptive Cartesian grid method, Chin. J. Theor. Appl. Mech. 37 (2005) 80–86.
[48] Y. Zhang, Numerical Simulation of Flow Around Airfoil Based on LBM and Cartesian Grid (Master Dissertation), School of aeronautics, Northwestern Polytechnical University, Xi'an, 2012.
[49] A.N. B, Numerical Study of the Flow Around Airfoil and Ice Accretion Based on LBM (Master Dissertation), School of aeronautics, Northwestern Polytechnical University, Xi'an, 2013.
[50] A.N. B, W.M. Sang, The numerical study of lattice boltzmann method based on different grid structure, Chin. J. Theor. Appl. Mech. 45 (5) (2013) 699–706, http://dx.doi.org/10.6052/0459-1879-12-333.
[51] R.Q. Jiang, Applications of LBM under High Reynolds Number (Master, Dissertation), Harbin Engineering University, Harbin, 2008.
[52] Z.L. Guo, C.G. Zheng, B.C. Shi, Non-equilibrium extrapolation method for velocity and boundary conditions in the lattice Boltzmann method, Chin. Phys. 11 (4) (2002) 366–374, http://dx.doi.org/10.1088/1009-1963/11/4/010.
[53] R.W. Mei, D.Z. Yu, W. Shyy, An accurate curved boundary treatment in the lattice Boltzmann method, J. Comput. Phys. 155 (2) (1999) 307–330, http://dx.doi.org/10.1006/jcph.1999.6334.
[54] Y. Chen, Z.H. Xia, Q.D. Cai, Lattice boltzmann method with tree-structured mesh and treatment of curved boundaries, Chin. J. Comput. Phys. 27 (1) (2010) 23–30.
[55] Z.L. Guo, C.G. Zheng, B.C. Shi, An extrapolation method for boundary conditions in lattice Boltzmann method, Phys. Fluids 14 (6) (2002) 2007–2010, http://dx.doi.org/10.1063/1.1471914.
[56] S. Arun, A. Satheesh, Analysis of flow behavior in a two sided lid driven cavity using lattice Boltzmann technique, Alex. Eng. J. 54 (4) (2015) 795–806, http://dx.doi.org/10.1016/j.aej.2015.06.005.

Please cite this article as: B. An, J.M. Bergadà, F. Mellibovsky et al., New applications of numerical simulation based on lattice Boltzmann method at high Reynolds numbers, Computers and Mathematics with Applications (2019), https://doi.org/10.1016/j.camwa.2019.10.002.